IN-02
153134
p- 82

NASA Contractor Report 191088

A Study of the Accuracy of Neutrally Buoyant Bubbles Used as Flow Tracers in Air

Michael F. Kerho
University of Illinois
Urbana, Illinois

March 1993

Prepared for
Lewis Research Center
Under Contract NAG3-1134

ORIGINAL CONTAINS
COLOR ILLUSTRATIONS

National Aeronautics and
Space Administration

A STUDY OF THE ACCURACY OF NEUTRALLY BUOYANT BUBBLES USED AS FLOW TRACES IN AIR

Michael F. Kerho
University of Illinois
Urbana, Illinois 61801

ABSTRACT

Research has been performed to determine the accuracy of neutrally buoyant and near neutrally buoyant bubbles used as flow tracers in air. Theoretical, computational, and experimental results are presented to evaluate the dynamics of bubble trajectories and factors affecting their ability to trace flow-field streamlines. The equation of motion for a single bubble was obtained and evaluated using a computational scheme to determine the factors which affect a bubble's trajectory. A two-dimensional experiment was also conducted to experimentally determine bubble trajectories in the stagnation region of a NACA 0012 airfoil at 0° angle of attack using a commercially available helium bubble generation system. Physical properties of the experimental bubble trajectories were estimated using the computational scheme. These properties included the density ratio and diameter of the individual bubbles. The helium bubble system was then used to visualize and document the flow field about a 30° swept semispan wing with simulated glaze ice. Results were compared to Navier-Stokes calculations and surface oil flow visualization. The theoretical and computational analysis have shown that neutrally buoyant bubbles will trace even the most complex flow patterns. Experimental analysis revealed that the use of bubbles to trace flow patterns should be limited to qualitative measurements unless care is taken to ensure neutral buoyancy. This is due to the difficulty in the production of neutrally buoyant bubbles.

TABLE OF CONTENTS

NOMENCLATURE

Symbol	Description
a_c	centripetal acceleration of particle-bubble
b	model span
c	model free-stream chord
C_D	particle-bubble drag coefficient
D	particle diameter
Fr	Froude number, $U_\infty/\sqrt{cg}$
g	acceleration due to gravity
g_v	acceleration due to gravity vector
K	nondimensional inertial parameter, $\sigma D^2 U_\infty/18c\mu$
m	mass of the particle-bubble
p	static pressure
p_o	dynamic pressure
r	radial distance, bubble radius
$\hat{r}$	unit vector in radial direction
R	gas constant
Re_p	particle or bubble slip Reynolds number, $(\rho D U_\infty/\mu)\lvert\overline{v}_p - \overline{v}_f\rvert$
Re	free-stream Reynolds number, $\rho c U_\infty/\mu$
T	temperature
t	time
$\bar{t}$	nondimensional time, tU_∞/c
u	streamwise velocity component
U_∞	free-stream velocity

v	velocity due to vortex, normal velocity component
v_f	fluid velocity vector
v_p	particle-bubble velocity vector
x_p	particle-bubble position vector
α	model angle of attack
γ	bubble solution surface tension
Γ	vortex strength
$\hat{\theta}$	unit vector in θ direction
ρ_{bfs}	bubble solution density
ρ	fluid density
σ	particle-bubble density
τ	bubble wall thickness
μ	fluid viscosity

Superscripts:

$\bar{\ }$	nondimensional
$\dot{\ }$	derivative with respect to nondimensional time

CHAPTER ONE

Introduction:

The understanding of complex fluid-dynamic processes has always been eased by insight manifested through physical visualization of the flow field. Flow visualization differs from other forms of experimentation in that it depicts certain aspects of a flow field in a manner conducive to a better physical understanding of the overall process than that provided by quantitative experimentation alone. The common expression, "A picture is worth a thousand words," relates the global nature of information obtained through the visualization of a fluid dynamic process. "Most fluids, gaseous or liquid, are transparent media, and their motion remains invisible to the human eye during direct observation; as a result, in order to be able to recognize the motion of the fluid, one must provide a certain technique by which the flow is made visible."[1]

The most common method of flow visualization in air is smoke, which in steady flow can reveal the flow-field streamlines. For a complex unsteady flow field however, the physically small nature and large concentration of smoke particulate make it impossible to follow individual particles and obtain pathlines. A complex unsteady or turbulent flow field will also tend to disperse smoke in such a manner so as to allow visualization of overall dynamics, i.e. wakes, vortices, and separated flows, but individual pathlines cannot be visualized.[2] The ability to trace individual pathlines provides valuable insight into the physics of an intricate flow field.

In order to obtain pathlines in an unsteady or turbulent flow field, a much larger individual particle size and lower concentration is needed than that provided, for example by smoke in air, or dye in water. For water, this can be overcome through the use of small hydrogen bubbles as flow tracers. Air, on the other hand, due to its low density makes the use of large particulate more difficult. A particle must be large enough to allow itself to be followed visually, but light enough to respond to gradients in the flow field. This can be accomplished through the use of helium filled soap bubbles. Whereas smoke provides particulate matter on the order of 1μm to 5μm[1], nearly neutrally buoyant helium bubbles can be generated on the order of 1mm to 4.75mm[3]. The bubbles are large enough to be followed individually throughout the flow field, but still provide a particle density close to that of air. The "neutral" density of the bubble allows it respond to changes in the flow field and trace streamlines. To date, however, no in depth study has been performed so as to determine the accuracy with which the helium bubbles trace the streamlines of a steady flow, or the pathlines of an unsteady flow.

The purpose of this study is to provide the first published research as to the accuracy of helium bubbles used as flow tracers in air. The current investigation involved computational, experimental, and application phases. A computational model was employed to calculate individual helium bubble trajectories in a potential flow field. The computational model was used to provide a better understanding of the forces imparted on a bubble by the surrounding fluid and the effect they have upon its trajectory. Additionally, a 2-D experimental investigation was conducted where the trajectories of individual bubbles were acquired in the stagnation region of a NACA 0012 airfoil at 0° angle of attack. These experimental results are then compared to potential streamlines of an equivalent flow field and trajectories obtained from the computational model. After the 2-D investigation, the helium bubble visualization system was used to document the separated region on the upper surface of a 3-D swept, semi-span model with a NACA 0012 section and simulated ice. Results from this 3-D investigation are compared to Navier-Stokes simulations performed for the NACA 0012 swept model.

Review Of Literature:

The first classic series of lectures on the properties of soap bubbles was given by C. V. Boys in 1889 and later published in 1959[4]. A treatise on the subject written for laymen, Boys documents several interesting experiments dealing with soap bubbles and soap films. The first mention of bubbles employed for flow visualization in air was by C. N. H. Lock in a Technical Report of the Aeronautical Research Committee of London in 1928[5]. In the report, Lock details the use of "streamers" of small strings of cotton with a ball of wool at the end to document the flow around an airscrew in the "vortex ring state." In his concluding remarks, Lock compares his results to those of a fellow researcher by the name of Townend. In Townend's study, flow visualization of the region in question was obtained by injecting soap bubbles into the flow field. Townend devised an apparatus which produced a steady stream of bubbles filled with coal gas; by adjusting the size of the bubbles the density could be made roughly equal to that of air. Lock then describes a promising future for the use of neutrally buoyant bubbles as flow tracers in air if they could be properly photographed.

The next published account of the use of soap bubbles employed for aerodynamic flow visualization was not until 1936 by Redon and Vinsonneau[6] at Marseille, France. Except for work published by Kampe de Feriet in 1938[7], the use of bubbles for aerodynamic flow visualization disappeared until the work of E. Pounder[8] in 1956 to study the flow about various parachute canopies. Helium filled soap bubbles were injected into the air passing the parachute and photographed. The bubbles were said to be dynamically indistinguishable from the air surrounding them. In 1961, Owen[9] also generated small bubbles to study the flow within a cylindrical vortex tube.

A modern commercial helium bubble generation system was not developed until 1971 by Hale et. al[10,11]. The reports published on the development of the bubble generation system include tests performed to visualize tip vortices generated by a semispan wing and the streamlines of a 2-D Karman-Trefftz airfoil. An investigation as to the accuracy of the method was presented by calculating the potential flow field about the 2-D Karman-Trefftz airfoil and then pictorially comparing to streak photographs of the bubbles. By this method, the bubbles were shown qualitatively to compare well to the streamlines of the potential flow field.

Using this commercially available system, Klimas documented the flow field of an opening parachute in 1973[8]. Empey and Ormiston employed the helium bubble system to visualize the flow field of a helicopter in ground effect in 1974[12]. The system revealed well defined ground and trailing vortices. In 1976, Colladay and Russell[13] performed flow visualization studies of discrete hole-film cooling. The highly turbulent nature of the flow field involved in this type of cooling process dictated the use of large particulate flow tracers. The helium bubble system provided well defined streakline photographs of the complex flow field.

The uniqueness and general ease of implementation of a bubble generation system for flow visualization has lent itself to the diverse range of applications related above. From the visualization of the highly three-dimensional flow field of a close coupled canard studied by Hale et. al[14], to quantitative flow-field measurements using stereo photography to determine the 3-D fluid motion in an engine cylinder[15].

CHAPTER TWO

Theory of Bubble Mechanics:

Particles injected into a flow field move relative to the surrounding fluid and have a finite response time to changes in that flow field. It is this relative motion of the helium bubbles to the surrounding fluid that is in question. The motion of a particle in an accelerating fluid has been a topic of study for centuries. Invoking Newton's second law, F=ma, the sum of the forces on a particle or body are equal to the bodies mass times its acceleration. Solving this second order differential equation will yield the particle position with time. Several assumptions must be made, however, before a useful equation of motion for a single bubble can be derived. These assumptions include that the physical size of a bubble and the concentration of the particles in the fluid be small enough that the bubbles have no effect upon each other or the surrounding flow field. The bubbles are also assumed to remain spherical throughout their trajectory; an assumption that may be violated as the bubble experiences large transverse pressures and accelerations.

The equation of motion for a single particle is given by Soo[16] and Rudinger[17]:

$$m\frac{d^2x_p}{dt^2} = \text{Drag} + \text{Gravity} + \text{Pressure} + \text{Apparent Mass} + \text{Basset Force} \tag{1}$$

The individual terms on the right hand side take the form:

$$\text{Drag} = \frac{1}{2}\rho C_D S\,|v_f - v_p|\,(v_f - v_p)$$

$$\text{Gravity} = mg_v$$

$$\text{Pressure} = -\frac{\pi D^3}{6}\nabla p$$

$$\text{Apparent Mass} = \frac{1}{2}\frac{m}{\sigma}\rho\,(\dot{v}_f - \dot{v}_p)$$

$$\text{Basset Force} = 9m\sqrt{\frac{\mu\rho}{\pi D^2\sigma^2}}\int_0^t \frac{\dot{v}_f(t') - \dot{v}_p(t')}{\sqrt{t - t'}}\,dt' \tag{2}$$

The viscous drag term uses the empirical C_D expression of Langmuir and Blodgett as used by Bragg[18] and is based upon the slip velocity between the particle and local fluid. The C_D expression of Langmuir and Blodgett is valid for particle Reynolds numbers from 1 to 100. The apparent mass term represents the force needed to accelerate the mass of the fluid displaced by the accelerating sphere. The Basset force[19] represents the resistance due to the deviation of the flow field around the sphere from that for steady flow based upon the past relative acceleration of the particle. An integral term, the Basset force decays exponentially with the particle's history.

For most trajectory analysis, such as a water droplet or particulate matter, the ratio of the fluid density ρ, to that of the particle density σ, is very small. This fact, coupled with the generally small physical size of the individual particles, means only the viscous drag term need be retained. Due to the near neutral buoyancy of the helium bubbles however, and their much larger physical size, these terms should be retained. Substituting the relationships for the individual terms given in (2), equation (1) becomes:

$$m\frac{d^2x_p}{dt^2} = \frac{1}{2}\rho C_D S\,|v_f - v_p|\,(v_f - v_p) + mg_v - \frac{\pi D^3}{6}\nabla p + \frac{1}{2}\frac{m}{\sigma}\rho\,(\dot{v}_f - \dot{v}_p)$$
$$+\,9m\sqrt{\frac{\mu\rho}{\pi D^2\sigma^2}}\int_0^{t}\frac{\dot{v}_f(t') - \dot{v}_p(t')}{\sqrt{t - t'}}\,dt' \tag{3}$$

Nondimensionalizing the above terms by the free-stream properties and chord length, and dividing through by the particle mass yields:

$$\ddot{\bar{x}}_p = \frac{3}{4}\frac{c\rho C_D}{D\sigma}|\bar{v}_f - \bar{v}_p|(\bar{v}_f - \bar{v}_p) + \frac{g_v}{g}\frac{gc}{U_\infty{}^2} - \frac{\rho}{\sigma}\overline{\nabla p} + \frac{1}{2}\frac{\rho}{\sigma}(\dot{\bar{v}}_f - \dot{\bar{v}}_p)$$

$$+\,9\sqrt{\frac{\mu\rho c}{\pi D^2\sigma^2 U_\infty}}\int_0^{\frac{\bar{t}c}{U_\infty}}\frac{\dot{\bar{v}}_f(t') - \dot{\bar{v}}_p(t')}{\sqrt{\bar{t} - \bar{t}'}}\,d\bar{t}' \tag{4}$$

Equation (4) presents three nondimensional parameters upon inspection. These parameters include the inertia parameter K, a nondimensional particle mass[18] given by $K=\sigma D^2 U_\infty/18c\mu$, the Froude number Fr, a ratio of inertial to gravitational forces given by $Fr=U_\infty/(cg)^{1/2}$, and the particle Reynolds number given by

$Re_p=(\rho D U_\infty/1\mu)|v_p - v_f|$. Substituting for these parameters and performing a little algebraic manipulation, the final form of the trajectory equation becomes:

$$\ddot{\bar{x}}_p = (1+\frac{1}{2}\frac{\rho}{\sigma})\left[\frac{1}{k}\left(\frac{C_D Re_p}{24}\right)(\bar{v}_f - \bar{v}_p) + \left(\frac{1}{Fr^2}\right)\frac{g_v}{g} - \frac{\rho}{\sigma}\overline{\nabla p} + \frac{1}{2}\frac{\rho}{\sigma}\dot{\bar{v}}_f\right]$$

$$+(1+\frac{1}{2}\frac{\rho}{\sigma})\left[9\sqrt{\frac{\rho^2 c^2}{\pi D^2 \sigma^2 Re}}\int_0^{\frac{\bar{t}c}{U_\infty}}\frac{\dot{\bar{v}}_f(t') - \dot{\bar{v}}_p(t')}{\sqrt{\bar{t} - \vec{t}}}d\vec{t}\right] \qquad (5)$$

For a known flow field, equation (5) can be used to calculate the trajectory of a helium bubble or particle for various diameters and density ratios, i.e. neutrally buoyant, buoyant, and heavy. A computational scheme developed by Bragg[18] to calculate water droplet impingement trajectories has been modified to include the extra terms present in equation (5). This scheme uses the Theordorsen method to calculate the potential flow field about an airfoil. The velocities from these calculations are substituted into equation (5) which is solved for bubble positions and velocities. The use of this computational program allows a much better understanding of the physics involved as a bubble experiences flow-field gradients and provides a means of comparison to experimentally obtained trajectories.

A particle following a flow-field streamline is acted upon only by pressure and gravity forces. This particle can be thought of as an arbitrary volume of mass having the same density as the fluid medium. The pressure forces imposed upon the arbitrary volume of mass will cause it to perfectly trace the streamlines of a steady flow field, or the pathlines of an unsteady flow field. For a neutrally buoyant particle the pressure forces exactly balance the inertial forces present in equation (3). On the other hand, a non-neutrally buoyant particle will not follow the flow-field streamlines because there exists an imbalance between the pressure and inertial forces. As a result, slip between the particle and the surrounding flow-field occurs. Referring to the dimensional terms described in (3), note that all terms on the right hand side except the pressure and gravity term are dependent either on slip velocities or slip accelerations. The gravity term containing the Froude number is balanced by buoyancy forces in the flow field. Therefore, in order to exactly trace streamlines or pathlines, the slip velocities and accelerations present in the inertial and viscous terms must be zero. Figure 1 shows several neutrally buoyant bubble trajectories versus flow-field streamlines.

From Fig. 1, the neutrally buoyant bubbles track the streamlines indentically as expected. Even in the stagnation region a neutrally buoyant particle will negotiate the considerable field gradients and trace streamlines. Since the program input can be varied for different bubble sizes and densities, the code can be used to study experimentally acquired 2-D bubble trajectories.

The effect of the density ratio upon an individual bubble trajectory can be determined by computing several trajectories while holding a constant diameter but varying the density ratio. The computer program allows the density ratio and diameter of a bubble to be chosen by the user. The density ratio of a bubble is defined as the ratio of the bubble's density to the free-stream air density. Therefore, density ratios less than one denote a bubble which would rise in a stagnant flow, where those greater than one would fall. Bubble's with density ratio less than one will be termed "buoyant," those with ratios greater than one, "heavy." The effect of density ratio upon a given trajectory is depicted in Fig. 2. An isocontour of the pressure coefficient calculated from the Theodorsen code is also shown underlying the computational trajectories in Fig. 2. The pressure contour is useful as it provides insight into pressure forces experienced by the bubble.

From Fig. 2, the "buoyant" bubble with a density ratio of 0.80 tracks outside the neutrally buoyant trajectory and away from the airfoil. The "heavy" bubble, however, with a density ratio of 1.33 tracks inside the neutrally buoyant trajectory and its inertia carries it in towards the airfoil. For both non-neutrally buoyant bubbles, the balance between the pressure and inertial forces in the trajectory equation has been lost. As a result, neither the "heavy" nor "buoyant" bubble follow a streamline. Examining the pressure isocontour, as the bubble approaches the stagnation region, it experiences an increasing pressure. If inertial forces are not large enough to provide a balance to the pressure forces, the bubble is drawn away from the airfoil. If, on the other hand, the inertial terms outweigh the pressure, the bubble will move towards the airfoil.

For bubbles with very low density ratios, the pressure force is so great that after moving away from the airfoil in the stagnation region, it will cross the streamlines again and be drawn towards the airfoil. This happens as it accelerates around the leading edge and experiences a decreasing pressure gradient towards the airfoil. This effect is not depicted in Fig. 2 since the density ratio is not sufficiently small enough.

The effect of the pressure gradients in the flow field and their impact upon various bubble trajectories as a function density ratio can also be studied by examining the bubble's velocity components in the stagnation region. The density ratio generates a similar effect upon a bubble's velocity as the effect observed upon the trajectory. A plot of the bubble streamwise velocity u/U_∞ for the same conditions as presented in Fig. 2 is shown in Fig. 3. From the previous discussion of the relationship of pressure to inertial forces and the effect various density ratios have upon a trajectory, a buoyant bubble is affected more by the pressure forces in the flow field than a heavy bubble. From Fig. 3, as the bubble approaches the stagnation region and experiences an increasing pressure force, the streamwise component of velocity for the buoyant bubble is shown to be less than that for the heavy. As the bubble accelerates around the leading edge and experiences a favorable pressure force, the buoyant bubble's streamwise component of velocity becomes greater than that for the heavy. As expected, the neutrally buoyant bubble's u/U_∞ lies between the buoyant and heavy bubble velocity values. Since the inertial forces are greater than the pressure for the heavy bubble, it is less effected by the pressure forces in the flow field.

The normal or y component of velocity for the same conditions used in Figs. 2 and 3 is given in Fig. 4. The buoyant bubble is shown to have a larger v/U_∞ than the neutrally buoyant bubble. Because the buoyant bubble crosses the streamlines and moves out away from the airfoil, its normal velocity should be greater than an equivalent neutrally buoyant bubble. The converse is true for the heavy bubble.

The computational and theoretical analysis of the equation of motion for a bubble has verified the assumption that a neutrally buoyant bubble will exactly trace flow-field streamlines. The sensitivity of the bubble to its density ratio has also been observed and has proven to be a dominant factor in determining the bubble's velocity and trajectory.

CHAPTER THREE

2-D Experimental Set-up and Procedure:

These experiments were conducted in the subsonic wind tunnel at the University of Illinois at Urbana-Champaign. The tunnel is an open return type with a 3 by 4 foot test section capable of operating from 0 to 165 mph at Reynolds numbers up to 1.5×10^6 per foot. Honeycomb and four turbulence screens located in the settling chamber provide a test section turbulence level as low as 0.05% for an empty tunnel.

The 2-D experiment involved video taping individual bubbles moving in a 2-D laser sheet near the stagnation region of a NACA 0012 airfoil. The NACA 0012 model used for the experiment had a chord of 0.5334 meters and was mounted vertically in the test section. Helium bubbles were generated using a commercially available system. The bubbles are approximately 1mm to 4.75mm in diameter and are formed by injecting helium into a special soap film through a concentric tube arrangement[11]. A dual generator system was used with the bubble producing "head" being contained within "vortex filters" supplied by the same vendor. The heads and filter set-up were located in the tunnel settling chamber just aft of the anti-turbulence screens. The bubble generation system was set according to the calibration data received from the commercial vendor. The bubbles were illuminated by a 4-watt argon laser sheet approximately 2mm thick projected perpendicular to the airfoil surface.

A KODAK Ektapro motion analysis system was used to video tape and quantize the individual bubbles entering the laser sheet in the stagnation region of the airfoil. The system consisted of an Ektapro 1000 image processor and Ektapro intensified imager. The system was connected to a 386-type PC. The image processor was operated at 1000 frames per second with an imager gain of 73 and a gate time of 70μs. A 200mm lens was used providing a pixel resolution of approximately 0.60mm. After storing the images on digital video tape, the image processor was controlled by the PC using a software package called Motion Pro. The Motion Pro software controlled the imager and allowed a frame by frame analysis by which individual bubbles could be tracked for distances on the order of 35mm to 25cm depending upon the pixel resolution required and free-stream velocity. A schematic of the test set up is shown in Fig. 5.

The intensified imager was placed on the top of the test section looking down and leveled so as to provide a picture in the same plane as the 2-D laser sheet. The imager was focused on the laser sheet and covered a small field of view about 35mm^2. Only bubbles within the sheet were illuminated and recorded by the imager thereby insuring 2-D motion in the plane of the sheet. Misalignment in the geometry of the set-up could be a possible source for error in this experiment. Error introduced in the geometrical alignment of the imager, laser sheet, or airfoil would introduce error in the calculations of bubble velocities and positions. The laser sheet and imager picture must be in the same plane in order to extract accurate velocity or coordinate data from the digital video recording. A more detailed error analysis is given after the 2-D results and discussion section. Markings on the airfoil at the stagnation point and 5% chord locations were illuminated by the laser sheet and provided a reference length for the velocity and coordinate calculations. A free-stream velocity of 18 m/s (Re=640,000) was chosen as it provided an acceptable number of data frames for a bubble passing through the field of view.

2-D Experimental Results and Discussion:

Approximately fifty individual bubbles were tracked using the Ektapro video system. Due to the nature of the high speed digital system, a single digital video tape allowed for approximately 30 seconds of taping. During this time period three to four bubbles would enter the 2-D laser sheet in the stagnation region and be recorded. Reduction of the 30 second digital tape required two to the three hours of frame by frame analysis. Trajectory data obtained was then further reduced and normalized by free-stream conditions. Velocity data were calculated using a finite difference approach knowing the bubble position and the time between frames. In order to simplify analysis and presentation, reported bubble positions are averaged between the experimentally acquired locations; note that this position corresponds to the location at which the velocity was calculated using the finite difference technique mentioned above. The actual positions are tabulated with the velocity calculations and given in Appendix A.

A comparison of several typical bubble trajectories to flow-field streamlines is given in Fig. 6. From Fig. 6, the bubble trajectories are shown to deviate somewhat from the flow-field streamlines; the only exception being the bubble trajectory nearest the stagnation streamline at y/c=0.005. The general trend of the helium bubbles was to cross over the streamlines, moving away from the airfoil. This tendency to cross over and move outside of the streamlines was observed with the majority of the experimental trajectories acquired. No bubble trajectories were observed to cross and track inside of the streamlines, moving towards the airfoil.

Each bubble trajectory was computationally matched using the program described earlier. Since the helium bubbles were not tracing streamlines, they could not be neutrally buoyant. The trajectory equation is a balance between pressure, inertial, and viscous forces; subsequently, more than one combination of density ratio and diameter is possible for a given trajectory. As a result, when individual experimental trajectories were matched, the diameter of the bubble was varied from 1mm to 5mm while changing the density in order to "match" the experimental trajectory. The trajectory was "matched" by plotting the experimental data versus the computational on an enlarged scale and visually identifying the best diameter-density ratio combinations. Fig. 7 depicts a typical comparison of the computational and experimental trajectories. Plots of additional computational bubble trajectories versus experimental data are given in Appendix B.

From Fig. 7, the three different diameters and corresponding density ratios fit the experimental trajectory well. Estimated density ratios for the bubble range from 0.714 to 0.833. It was observed that as the diameter of the bubble decreased, a smaller density ratio was required to match the trajectory. Since the pressure force goes as the radius cubed, as the diameter of the bubble decreases, the pressure force on the bubble is reduced and a more buoyant bubble is required to match the experimental trajectory. An isocontour of the pressure coefficient calculated from the Theodorsen code is also shown underlying the trajectory in Fig. 7. Since the bubble was shown to be "buoyant" and track over and outside the streamline, the pressure forces in the trajectory equation are greater than the inertial forces. Examining the pressure isocontour in the same manner as was done in the bubble mechanics section, as the bubble approaches the stagnation point, it experiences an increasing pressure. If inertial forces are not sufficiently large enough as to provide a balance to the pressure forces, the bubble is drawn outwards away from the airfoil. Only a neutrally buoyant particle can produce an exact balance of the forces needed to follow flow-field streamlines.

Experimental bubble velocities were also compared to velocities at points along a streamline. For this comparison, a streamline was chosen that coincided with the initial position of a bubble trajectory. Velocities at points on the streamline are compared to the experimental bubble velocities at a given x/c. Figure 8 depicts a comparison of the streamwise component of velocity for bubble #33 versus the streamwise velocity on the streamline. The estimated density ratio for bubble #33 is $\sigma/\rho=0.658$. The plot depicts velocity versus position on the left axis and the experimental trajectory and streamline on the right axis. From Fig. 8, examining the experimental trajectory and noting the estimated density ratio, the bubble is seen to be buoyant. Therefore, as the bubble approaches the stagnation region and experiences an increasing pressure force, its streamwise component of velocity is less at a given x/c than the velocity on the streamline. As the bubble begins to accelerate around the leading edge, its velocity increases beyond that of a point on the streamline. Due to the small number of experimental data points, however, the resolution as compared to the computational data is poor.

A comparison of the normal or y component of velocity for bubble #33 versus a streamline is shown in Fig. 9. The plot depicts velocity versus position on the left axis and the experimental trajectory and streamline on the right axis in the same format as used for Fig. 8. Again, since the bubble is buoyant and tracks outside the streamline, its normal velocity is greater at a given x/c than the corresponding point on the streamline for $x/c < 0$. At $x/c >$

0, the normal velocity appears to track with that of the streamline. By examining the trajectory position data, at x/c > 0 the bubble and streamline appear to follow parallel paths. The normal component of velocity should differ only if the trajectories are not parallel. The trends observed in the bubble velocity data are the same as discussed in the theory of mechanics section. The dominant factor in determining a bubble's trajectory is the pressure force.

After matching the experimental runs with computational trajectories, a density ratio and diameter for each run was computed so as to obtain an estimate of the experimental bubble's properties. After obtaining estimates for the experimental data, probability distributions for the diameter and density ratio were calculated. Histograms of diameter and density ratio are shown in Figs. 10 and 11. Figures 10 and 11 provide an estimate for the average bubble diameter and density ratio. The average diameter being approximately 3.75mm and the average density ratio approximately 0.65. The distributions are gaussian in appearance although the deviation is rather large.

Settling velocities were calculated for different diameters and density ratios in order to determine if the computational estimates were reasonable. The settling velocity is computed by determining the bubble's terminal velocity for free fall or rise in a stagnant fluid. A method described by Clift et al.[20] was used to obtain an expression for the terminal velocity based upon bubble diameter and density ratio. A plot of the bubble terminal velocity versus density ratio is shown in Fig. 12 for various diameters. For the average estimated diameter and density ratio of 3.75mm and 0.65, Fig. 12 predicts a rise velocity of approximately 0.3ft/s ±4%. Although on the high side, this estimate is in the range of physically acceptable values. When the bubbles are produced by the generator, it is difficult to visually determine the percentage of bubbles which are neutrally buoyant, or approximately neutrally buoyant. As the bubbles are generated in the vortex filter, they are expelled with an initial velocity. After filling the room with bubbles, a velocity less than 0.3 ft/s is hard to distinguish unless the local room air is stagnant.

Another means of determining if the estimated density ratios and diameters are reasonable is to compute a bubble wall thickness. For a given density ratio and diameter, a wall thickness can be calculated. Soap bubble wall thicknesses can vary from 0.01μm to 1.3μm.[21] Knowing the bubble film density and assuming a surface tension, an equation relating density ratio to diameter and wall thickness can be derived from a simple mass balance. The surface tension of the bubble solution is needed to calculated the pressure and density of the helium inside the bubble. A value for the surface tension can be assumed having little effect upon the accuracy of the calculation due to the relatively low pressure difference across the bubble wall. An order of magnitude estimate is all that is required.

Equating the total mass of the helium bubble to the sum of the mass of its constituents:

mass of bubble = mass of bubble solution + mass of helium

$$\frac{4}{3}\pi r^3\sigma = \frac{4}{3}\pi\left(r^3 - (r - \tau)^3\right)\rho_{bfs} + \frac{4}{3}\pi(r - \tau)^3\rho_{helium} \tag{6}$$

Performing a little algebraic manipulation and dividing through by the density of air, ρ:

$$\frac{\sigma}{\rho} = \frac{1}{\rho}\left[\left(1 - \frac{\tau}{D/2}\right)^3 (\rho_{helium} - \rho_{bfs}) + \rho_{bfs}\right]$$

$$\rho_{helium} = \frac{P_\infty}{RT} + \frac{4\gamma}{(D/2)RT} \tag{7}$$

Figure 13 shows the estimated bubble diameters and density ratios plotted with wall thicknesses calculated using equation (7). From Fig. 13, the estimated values indicate an average bubble wall thickness of 0.2μm to 0.3μm. These values are well within the limits of measured bubble wall thicknesses quoted by Isenberg[21]. The grouping of the data around this average value indicates a relatively constant wall thickness. If the wall thickness were shown to vary by a large amount from bubble to bubble, the ability to produce large numbers of bubbles having approximately the same density ratio would be questionable.

From the 2-D data obtained, the bubbles were generally shown to deviate somewhat from the streamlines. The effects of various density ratios upon the dynamics of the bubble motion indicate a strong relationship between flow-field pressure forces and bubble trajectories. Plots of the experimental trajectories and velocities agree well with trends observed in the theoretical development of the equation of motion as discussed in chapter two. The computational study of the data revealed that the majority of the bubbles recorded were buoyant having density ratios less than one. No bubbles were recorded having a density ratio greater than one. After an analysis of the bubble generation system itself, the range of "buoyant" density ratios and lack of "heavy" bubbles can be explained. Focusing on the vortex filter, an examination of the physics involved revealed that the filter does not totally screen out non-neutrally buoyant bubbles. A discussion of the vortex filter and its operation is offered in Appendix C.

The 2-D tests and analysis have shown that the use of the bubbles to trace flow patterns should be limited to qualitative measurements depending upon the accuracy required. If neutral buoyancy can be achieved, the bubbles will trace even the most complex flow patterns. For the case of Fig. 2 from chapter one, for example, where a buoyant, neutrally buoyant, and heavy bubble trajectory are compared, the percent error associated with the non-neutrally buoyant trajectories is not very large. From Fig. 2, the maximum deviation from the buoyant trajectory occurs at $x/c=0.20$. When compared to the neutrally buoyant trajectory at this location, the buoyant trajectory with a $\sigma/\rho=0.80$ is only 6.25% off, whereas the massive bubble with $\sigma/\rho=1.33$ is 13% off. The amount of error associated with a non-neutrally buoyant bubble is dependent, however, upon the magnitude of the pressure gradient. The larger the gradient, the larger the deviation. Although the analysis has shown that the current set-up produces a distribution of buoyant bubbles, the determination of the validity of data obtained through the use of the bubbles lies in the degree of accuracy required by the test. If only a global or qualitative measurement is required, the use of only neutrally buoyant bubbles is not imperative.

Error Analysis:

The accuracy of measurements made in this experiment rely heavily upon the proper alignment of the various instruments and airfoil. Geometrically, as discussed in the experimental set-up, the laser sheet and imager must be in the same plane. In turn, the plane of the laser sheet must be perpendicular the leading edge of the airfoil which is mounted vertically in the tunnel. Since velocity and position measurements are made by determining a linear scaling factor from some reference length in the field of view, a misalignment of the imager or laser sheet would affect the scaling factor. Instead of being linear, the scaling factor would become some nonlinear function dependent upon the actual alignment of the system and the relationship between the plane of the imager and laser sheet.

Misalignment in the angle of attack setting for the airfoil can be studied by comparing an experimental trajectory to streamlines produced at different angles of attack. Figure 14 shows an experimental trajectory and several streamlines generated for various angles of attack passing through the initial trajectory point. The y/c axis of this figure is expanded to obtain a more detailed comparison of trajectory shapes. The airfoil is not shown. This figure shows that by varying the angle of attack the streamlines could not be made to match the shape of the bubble trajectory; this implies that the model was properly aligned. If the streamlines could be made to match the trajectory by this process, the alignment of the model would be in question. The method used to set the angle of attack provided an accuracy of ±0.14°. From Fig. 14, this implies that to obtain a streamline even close to the trajectory, a gross misalignment of 1.5° is required.

Unsteadiness in the flow field as a result of the bubble generators could also be a possible source for measurement error. The bubble generators were placed on the floor of the settling chamber directly behind the anti-turbulence screens. A 1cm O.D. tube of approximately 1m in length was attached to the vortex filter-generator and placed so as to inject the bubbles at the centerline height of the tunnel. Flow-field fluctuations resulting from the vortex filter and head would be reduced by the contraction to the test section and lie below the center height of the tunnel and therefore below the measurement area. Small scale turbulence due to the injection tube would cause scatter in the individual trajectory points. The trajectories, however, appear well defined indicating that this was not the case. The fact that trajectory data from several bubbles was averaged would also reduce errors due to random fluctuations in the flow.

Pixel resolution for the field of view used was approximately 0.60mm. At this resolution, error bars for positional data in nondimensional form are ±0.0022 (x,y)/c. The corresponding error bars for velocity data nondimensionalized by the free-stream are ±0.065.

The assumption that the bubble remains spherical in shape is only a cause of possible error if the bubble is not neutrally buoyant. Error of this type would present itself if the shape of a non-neutrally buoyant bubble deviates from that of a sphere under large pressure gradients and accelerations. If a bubble deforms, the drag and pressure terms calculated by the trajectory equation will be in error. If the actual bubble is nonspherical for any portion of its trajectory, the computational estimate of this trajectory will not reflect the deviation. For the majority of a bubble's trajectory, the slip Reynolds numbers are small and the spherical assumption is justified. Very little has been done to study the various shape regimes a bubble in air experiences as a result of acceleration or velocity. Work has primarily concentrated on drops in air or bubbles in liquids.[20]

CHAPTER FOUR

Application of The Flow Visualization System:

The helium bubble flow visualization system was used to experimentally visualize and document the flow separation due to a simulated glaze ice accretion on a NACA 0012 semispan wing with 30° sweep. Results from the flow visualization are compared to Navier-Stokes computational simulations for different angles of attack.

The performance degradation of aircraft operating in icing conditions is a complex multi-variable problem and the resulting aerodynamic effects are an area of continued research. Experimental studies performed by Bragg et. al[22] have documented the aerodynamic performance of a 30° swept semi-span NACA 0012 model with simulated leading edge glaze ice. Corresponding Navier-Stokes computational studies by Kwon and Sankar[23] have attempted to predict this complex three-dimensional flow field. Agreement between the the experimental and computational studies has been favorable.[23,24]

The Navier-Stokes simulations performed on the swept NACA 0012 model have revealed a highly three dimensional separation bubble located behind the upper surface ice horn. The simulations depicted a trapped vortex with large spanwise velocities present in the separated region. The helium bubble system was employed to experimentally visualize and document the dynamics of the separation and trapped vortex. Due to the unsteady nature of this complex flow field, traditional methods of visualization could not be used. The large individual size and small concentration of particles generated by the helium bubble system provide the best means by which to document this flow field. A preliminary investigation of this flow field using the helium bubble system which includes streakline photographs of the bubbles is documented by Bragg et. al[22].

3-D Experimental Set-up and Procedure:

The model used for this portion of the test is a semispan wing with a simulated leading edge glaze ice accretion. The model has a free-stream chord of 0.4406m and a span of 0.8935m. A NACA 0012 airfoil section (in the plane perpendicular to the leading edge) was used on this 30° swept wing. The ice accretion used is a simulation of that measured on a NACA 0012 airfoil in the NASA Lewis Icing Research Tunnel. The icing conditions were a free-stream velocity of 63 m/s, $\alpha=4^\circ$, icing time of 5 minutes, volume median droplet diameter of 20 microns, LWC=2.1 g/m^3 and a temperature of -7.78 °C[22]. A two dimensional picture of the ice shape is shown in Fig. 15.

The same bubble injection system was used as in the 2-D experiment with the bubble generators located in the settling chamber aft of the anti-turbulence screens. The wing is sidewall mounted with the upper surface facing the bottom of the tunnel. The Ektapro Intensified Imager was placed underneath the tunnel and oriented to achieve a planform view of the “upper surface.” The bubbles are illuminated orthogonally through the sidewall plexiglass with the light projected along the span from tip to root. The light source for this portion of the test was a Quartz halogen lamp (DC spotlight) of 300,000+ candlepower. The test was conducted at a Reynolds number of 6.5 x 10^5. A schematic of the 3-D test set-up is shown in Fig. 16.

A 200mm lens was used providing a 25cm spanwise field of view; as a result, individual bubbles could not be tracked from root to tip. Therefore, three separate stations were taken along the span including the root, midchord, and tip. Bubbles were injected at the root for the inboard stations and at the midchord for the tip station. The image processor was operated at 1000 frames per second with a gain of 65-75 and gate times of 30μs or 70μs depending upon the amount of incident light being reflected by the bubbles and model.

3-D Results and Discussion:

Bubble trajectories were acquired at 4° and 8° angle of attack corresponding to the available Navier-Stokes simulation results. The Navier-Stokes simulations were for a Reynolds number of $1.5\text{x}10^6$, where the experiment was run at $6.5\text{x}10^5$. As stated in the 3-D experimental set-up, since the field of view was limited to approximately 25cm, three sets of trajectory data for each angle of attack were recorded. Each set corresponds to a different spanwise location including a root, midspan, and tip location. The midspan and tip stations were chosen to slightly overlap so as to check and assure continuity between stations. Since the trajectories from the overlapping stations were shown to agree well, a small gap was left between the root and midspan sections so as to allow a larger range of spanwise measurements to be made. For each station, five trajectories were recorded.

A sample of a single root, midspan, and tip trajectory is shown in Fig. 17 for the 4° angle of attack case. An outline of the semispan model is shown underlying the trajectory data. The trajectories in Fig. 17 depict a wavy motion as the bubble moves toward the tip of the model. This wavy motion is indicative of a three dimensional vortical trajectory viewed two dimensionally. In the actual flow, the bubbles enter and become trapped in the separation bubble generated by the upper surface ice horn and move towards the tip in a spiraling motion. Since data were obtained at 1000 frames per second, the time between data points was 0.001 seconds.

From the computational simulation of the iced wing flow field, the separation bubble for the 4° angle of attack case is seen to be relatively constant along the span ranging from the ice horn to approximately 20% of the free-stream chord. A plot of the computational results is shown in Fig. 18 depicting several trajectory simulations for the 4° case[24]. The separated region and strong vortical motion of the flow are clear.

Surface oil flow visualization was also performed on the model. The oil was placed on the model and the tunnel run until the flow pattern was established. The oil was mixed with a fluorescing additive and illuminated with an ultraviolet lamp. Photographs of the model were taken using a 35mm camera at a Reynolds number of 1.2×10^6. The surface oil flow visualization for the 4° angle of attack case is shown in Fig. 19. The reattachment of the leading edge vortex is clearly seen running parallel to the leading edge. Ahead of this line the vortical action is observed by the oil flowing toward the leading edge and outboard.[25] Spanwise flow near the tip is also evident.

From the experimental trajectories, the bubbles were seen to occupy a bounded region as they spiralled towards the tip. This bounded region represents a measure of the circulatory part of the separation bubble. Reattachment positions obtained through examination of the bubble trajectories present more of a qualitative analysis than a quantitative measurement. In order to deduce the extent of the separated region from the 4° experimental trajectory data, all the trajectories were plotted on a single figure with no symbols and only lines to connect the data points. Figure 20 shows these trajectories plotted with the computational separation reattachment line. Again a planform of the semispan model is shown underlying the plot. The region bounded by the bubble trajectories indicates the separation reattachment line to be at approximately the 15% free-stream chord position. The computational reattachment line is slightly further downstream at approximately 20% free-stream chord. The experimental reattachment position of 15% chord matches the surface oil flow visualization. Due to the relatively stagnant reattachment region of the separation bubble, one would not expect the helium bubbles to traverse the entire separated region depicted by the Navier-Stokes simulation.

Spanwise velocities in the separated region were generally shown to decrease as the helium bubble moved toward the tip. A histogram of the spanwise velocity taken over the entire span and normalized by U_∞ is shown in Fig. 21. The mean normalized velocity was shown to be 0.39 with a standard deviation of 0.17. The large standard deviation is expected since the flow field is unsteady.

For 8° angle of attack, the Navier-Stokes simulations depict the flow as being highly three dimensional with the separated region growing rapidly towards the tip. A plot of the 8° computational results is shown in Fig. 22 depicting several trajectory simulations[24]. Whereas for the 4° case, the bounds of the vortex induced flow region and reattachment line coincided, they are now different for the 8° case. The spanwise variation of the separation is much more pronounced than the 4° case and the reattachment line moves back to about the 80% chord position at y/b=0.60. The vortex induced flow region grows more gradually until the tip effects cause the vortex to move off the trailing edge around the three-quarter span location.

Surface oil flow was also performed for the 8° angle of attack case. The oil flow visualization is given in Fig. 23. From the figure, the flow is much more three dimensional than the 4° case. The separation is seen to grow rapidly towards the tip as shown in the computational result. The flow near the tip is shown to be almost parallel to the trailing edge behind the reattachment line. Ahead of the reattachment line the flow moves forward into the separated region.

The experimental trajectories indicate the same vortex trend seen in the computational simulation with the area of vortex induced flow growing rapidly towards the tip. Figure 24 shows the experimental trajectories plotted on a single graph; again no symbols have been used and only lines to connect the data points are shown so as to provide a clearer estimation of the bounded region. The computational simulation's reattachment line, vortex induced flow boundary, and a planform of the model are also shown. From Fig. 24, the experimental trajectories appear to exhibit the same spiraling motion towards the tip as seen in the 4° case. Near the root station(y/b=0.25 to 0.42) the vortex region grows from approximately the 24% to 40% free-stream chord positions for the computational simulation, whereas the bounded region containing the bubble trajectories remains relatively constant at the 21% free-stream chord position over the same span. At the midspan (y/b=0.45 to 0.70) and tip (y/b=0.58 to 0.85) stations, the computational simulation shows the vortex boundary to be growing rapidly from 45% at y/b=0.45 to the 80% free-stream chord position at y/b=0.70. The experimental results show the boundary to be approximately 30% at y/b=0.45, and 45% at y/b=0.75.

As seen in the 4° case, the spanwise velocity in the separated, vortex induced flow is seen to generally decrease as the bubbles move towards the tip. This is consistent with a vortex that is growing in diameter and becoming more diffuse as the wing tip is approached. A histogram of the spanwise velocity normalized by U_∞ is shown in Fig. 25. The normalized spanwise velocity for the 8° case is shown to be less than that recorded for the 4°. The 8° normalized mean of 0.28 also has a larger standard deviation of 0.23. The decrease in spanwise velocity might be due to the much more pronounced, but less localized, vortex induced flow.

The region of vortical flow is shown to be smaller in the experimental results than that predicted by the computational model. Near the tip, however, the restricted field of view did not allow the large vortical area shown in the computational results to be covered. Discrepancies between the computational and experimental results near the tip might also be due to the tip geometry used in the computational model. Also, as stated for the 4° case, due the actual nature of the relatively stagnant reattachment region of the separation bubble, one would not expect the helium bubbles to traverse the entire bounded region to the limits. The trends, however, predicted by the computations are present in the experimental trajectories and overall agreement between the two is good.

CHAPTER FIVE

Conclusions and Recommendations:

Research has been performed to determine the accuracy of helium bubbles used as flow tracers in air. The equation of motion for a single bubble was obtained and evaluated using a computational scheme to determine the factors which effect a bubble's trajectory. A two-dimensional experiment was conducted to experimentally determine bubble trajectories in the stagnation region of a NACA 0012 airfoil at 0° angle of attack using a commercially available helium bubble generation system. The computational scheme was used to estimate the physical properties of the experimental bubble trajectories. These properties included the density ratio and diameter of the individual bubbles. The helium bubble system was then used to visualize and document the flow field about a 30° swept semispan wing with simulated glaze ice.

The theoretical and computational results have shown, within the assumptions made in these analyses, that neutrally buoyant bubbles will exactly trace flow-field streamlines. From the equation of motion, all terms on the right hand side of the equation are dependent upon the slip velocity or acceleration between the bubble and the local free-stream except the pressure and gravity terms. The gravity term, however, is balanced by buoyancy forces in the flow field. Therefore, it is only the pressure and inertia which determine the trajectory of a particle following streamlines. If a bubble is not neutrally buoyant, the balance between pressure, gravity, and inertial forces is lost, and the bubble will not trace streamlines.

Computational analysis provided insight into the effects of various density ratios upon the bubble trajectory. Buoyant bubbles with density ratios less than one, were shown to track over and outside of streamlines moving away from the airfoil. Heavy bubbles with density ratios greater than one, on the other hand, track inside of the streamlines and are carried towards the airfoil by their inertia. The trajectory of an individual bubble was extremely sensitive to and most affected by its density ratio.

From the two dimensional experiment, several trajectories were acquired in the stagnation region of the NACA 0012 at 0° angle of attack through the use of a very high speed digital video motion analysis system. The trajectories were shown to deviate somewhat from the flow-field streamlines. Since the bubbles were not tracing streamlines, they could not be neutrally buoyant. The computational scheme was used to estimate individual bubble diameters and density ratios from the experimental trajectory data. All the estimated density ratios were in the buoyant range being less than one. An analysis of the bubble generation system itself provided an explanation for the large number of buoyant bubbles detected. The vortex filter was found to screen out only the heavy bubbles which have a net weight, and allow the buoyant as well as the neutrally buoyant bubbles to escape.

The two-dimensional experiment and analysis have shown that the use of the bubbles to trace flow patterns should be limited to qualitative measurements unless care is taken to ensure neutral buoyancy. The magnitude of the pressure gradients will determine the amount of deviation a non-neutrally buoyant bubble experiences. If neutrally buoyant bubbles can be produced and injected into a flow field, the bubbles will trace even the most complex of unsteady flows.

The three-dimensional experiment showed that although the current set-up produces a distribution of buoyant bubbles, the system provided good qualitative measurements of a complex separation dominated flow field. As a result, the determination of the validity of data obtained through the use of the bubbles lies in the degree of accuracy required by the test. If only a qualitative measurement is required, the use of only neutrally buoyant bubbles is not imperative and the current system provides an easily accessible means of flow visualization.

Future experimentation on the accuracy of the use of helium bubbles as flow tracers needs to include an experimental determination of the bubbles diameter and density ratio coupled with its trajectory data. An experimentation system able to deduce these fundamental bubble parameters could be used to develop a better bubble production process providing only neutrally buoyant bubbles. The ease of operation, flexibility, and non toxicity of the system point to a promising future. More work, however, needs to done in the development phase to provide a more reliable means of bubble production.

REFERENCES

1. Merzkirch, W., Flow Visualization, Second Edition, Academic Press, Inc., New York, 1987, pp. 1,14-51.

2. Goldstein, Richard J., Fluid Mechanics Measurements, Hemisphere Publishing Corp., New York, 1983, pp. 307-352.

3. Anonymous, "SAI Bubble Generator: Description and Operating Instructions" , Sage Action, Inc., New York, May 1988.

4. Boys, C. V., Soap Bubbles and The Forces Which Mold Them, Doubleday & Company, Inc., New York, 1959.

5. Lock, C. N. H., "Photographs of Streamers Illustrating The Flow Around An Airscrew In The Vortex Ring State", Aeronautical Research Council Reports and Memoranda 1167, April 1928.

6. Redon, M. H. and Vinsonneau, M. F., "Etude de l'ecolement de l'air autour d'une maquette", Aeronautique, Vol 18, No. 204, 1936.

7. Kampe de Feriet, J., "Some Recent Researches On Turbulence", Proceedings of the Fifth Int. Congress For Applied Mechanics, Cambridge, Mass., 1938, Wiley, New York, 1939.

8. Klimas, P. C., "Helium Bubble Survey of an Opening Parachute Flowfield", Journal of Aircraft, Vol. 10, No. 9, Sept. 1973, pp. 567-570.

9. Owen, F. S., Hale, R. W., Johnson, B. V., and Travers, A., "Experimental Investigation of Characteristics of Confined Jet-Driven Vortex Flows", United Aircraft Research Laboratory Report R-2494-2, AD-328 502, 1961.

10. Hale, R. W. , Tan, P., and Ordway D.E., "Experimental Investigation of Several Neutrally-Buoyant Bubble Generators For Aerodynamic Flow Visualization", Naval Research Reviews, June 1971.

11. Hale, R. W. , Tan, P., Stowell, R. C., and Ordway D.E., "Development of an Integrated System For Flow Visualization In Air Using Neutrally Buoyant Bubbles", SAI-RR 7107, Dec. 1971.

12. Empey, R. W., and Ormiston, R. A., "Tail-Rotor Thrust On A 5.5-Foot Helicopter Model In Ground Effect", paper presented at the 30th Annual National Forum of the American Helicopter Society, No. 802, Washington, D.C., May 1984.

13. Colladay, R. S., and Russell, L. M., " Streakline Flow Visualization of Discrete Hole Film Cooling For Gas Turbine Applications", Journal of Heat Transfer, Vol. 98, No. 2, May 1976, pp. 245-256.

14. Hale, R. W., Tan, P., Ordway, D. E., "Prediction of Aerodynamics Loads on Close-Coupled Canard Configurations - Theory and Experiment", SAI-RR 7702, July 1977.

15. Kent, J. C., and Eaton, A. R., "Stereo Photography of Neutral Density He-Filled Bubbles For Fluid Motion Studies In An Engine Cylinder", Applied Optics, Vol. 21, No. 5, March 1982, pp 904-912.

16. Soo, S., L., <u>Fluid Dynamics of Multiphase Systems</u>, Blaisdell Publishing Company, Toronto, 1967, PP. 31-43.

17. Rudinger, G., "Flow of Solid Particles in Gases", AGARDograph No. 222, 1967.

18. Bragg, M. B., "Rime Ice Accretion and its Effect on Airfoil Performance", NASA CR 165599, March 1982.

19. Basset, A. B., <u>A Treatise on Hydrodynamics</u>, Volume Two, Deighton, Bell, and Co., 1888, pp 285-297.

20. Clift, R., Grace, J. R., and Weber, M. E., <u>Bubbles, Drops, and Particles</u>" Academic Press, New York, 1978.

21. Isenberg, C. , "<u>The Science of Soap Films and Soap Bubbles</u>", Tieto Ltd., England, 1978.

22. Bragg, M. B., Khodadoust, A., Soltani, R., Wells, S, and Kerho, M., "Effect of a Simulated Ice Accretion on the Aerodynamics of a Swept Wing", AIAA 91-0442, paper presented at the 29th Aerospace Sciences Meeting, Reno, Nevada, Jan. 7-10, 1991.

23. Kwon, O.J. and Sankar' L.N.,"Numerical Study of the Effects of Icing on Fixed and Rotary Wing Performance", AIAA 91-0662, paper presented at the 29th Aerospace Sciences Meeting, Reno, Nevada, Jan. 7-10, 1991.

24. Potapczuk, M. G., Bragg, M.B., Kwon, O.J., and Sankar, L.N., "Simulation of Iced Wing Aerodynamics", NASA TM 104362 , also prepared for the 68th AGARD Fluid Dynamics Panel Specialists Meeting, Toulouse, France, April 29-May 1, 1991.

25. Bragg, M.B., Khodadoust, A., Soltani, R., Wells, S, and Kerho, M.,"Aerodynamic Measurements on a Finite Wing With Simulated Ice", AIAA 91-3217, paper presented at the 9th Applied Aerodynamics Meeting, Baltimore, MD, Sept. 23-25, 1991.

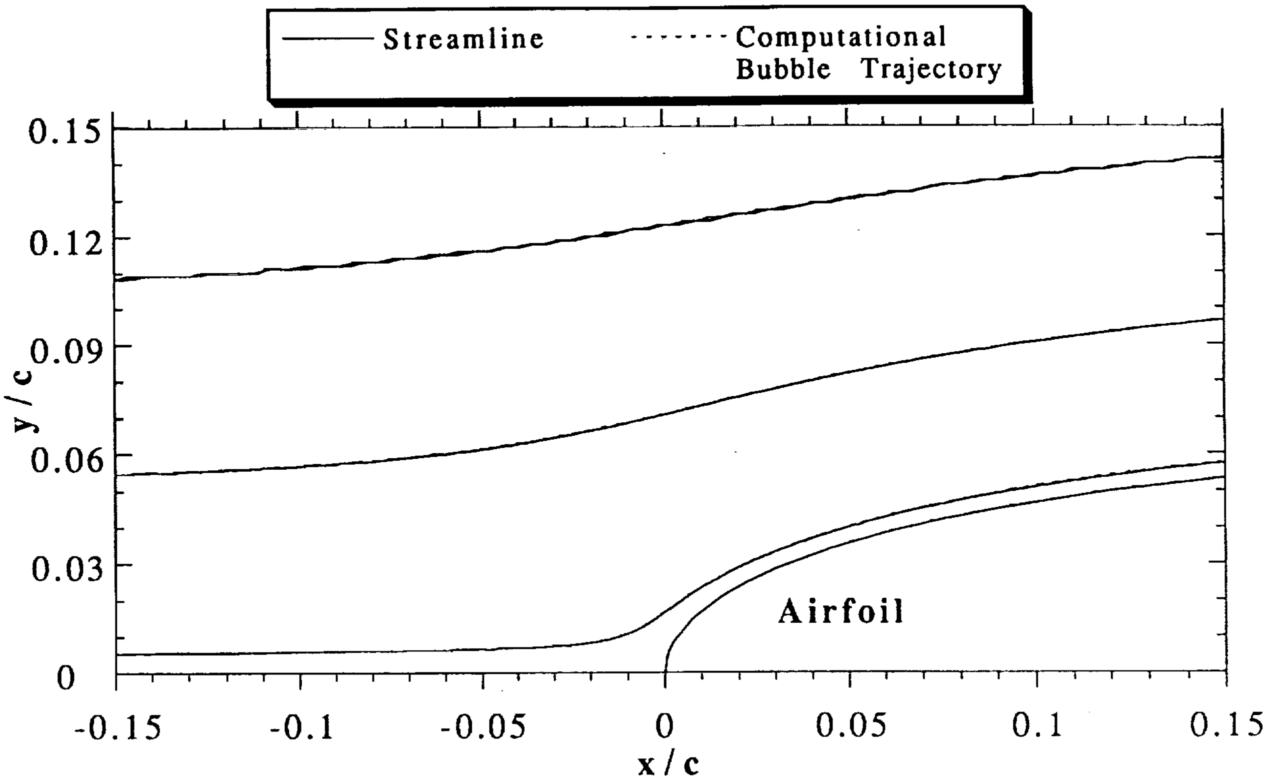

Fig. 1: Comparison of computational bubble trajectories to potential streamlines for a NACA 0012, α =0°, and Re = 6.4×10^5.

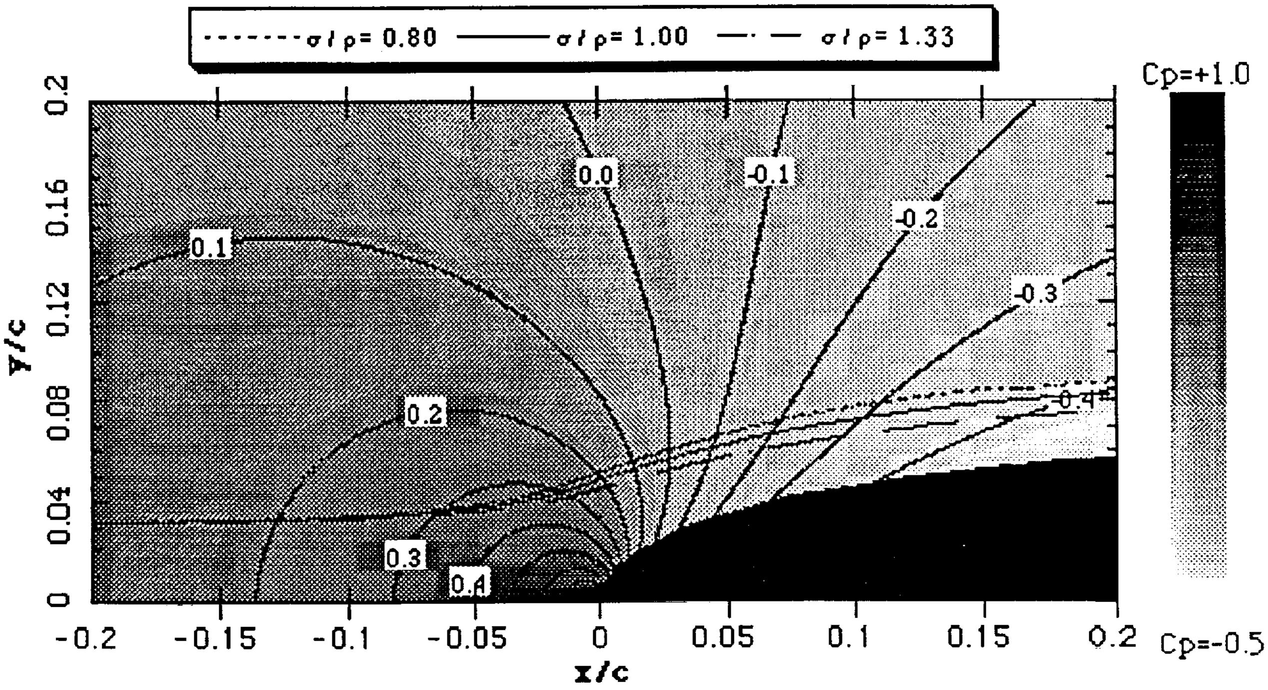

Fig. 2: The effect of density ratio on a computational bubble trajectory for a diameter of 3.0mm.

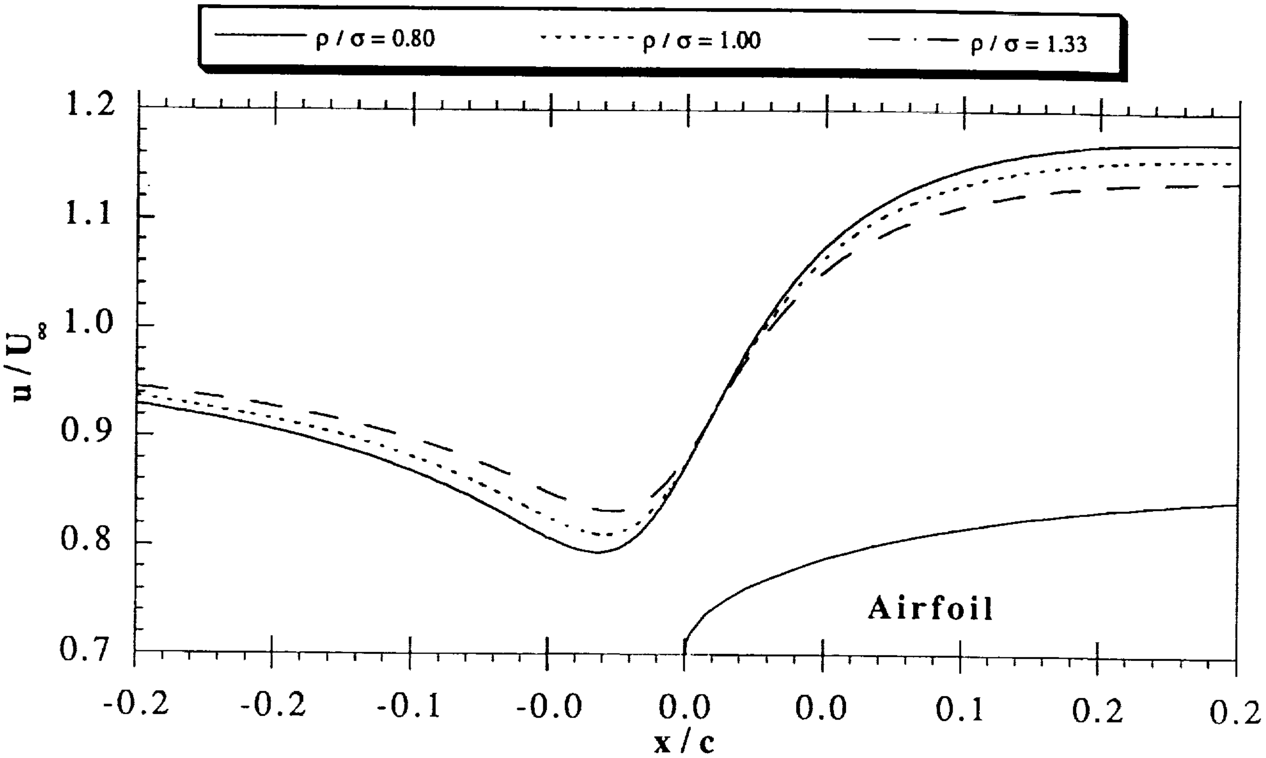

Fig. 3: The effect of density ratio on u/U∞ for a computational bubble trajectory for a bubble diameter of 3.0mm.

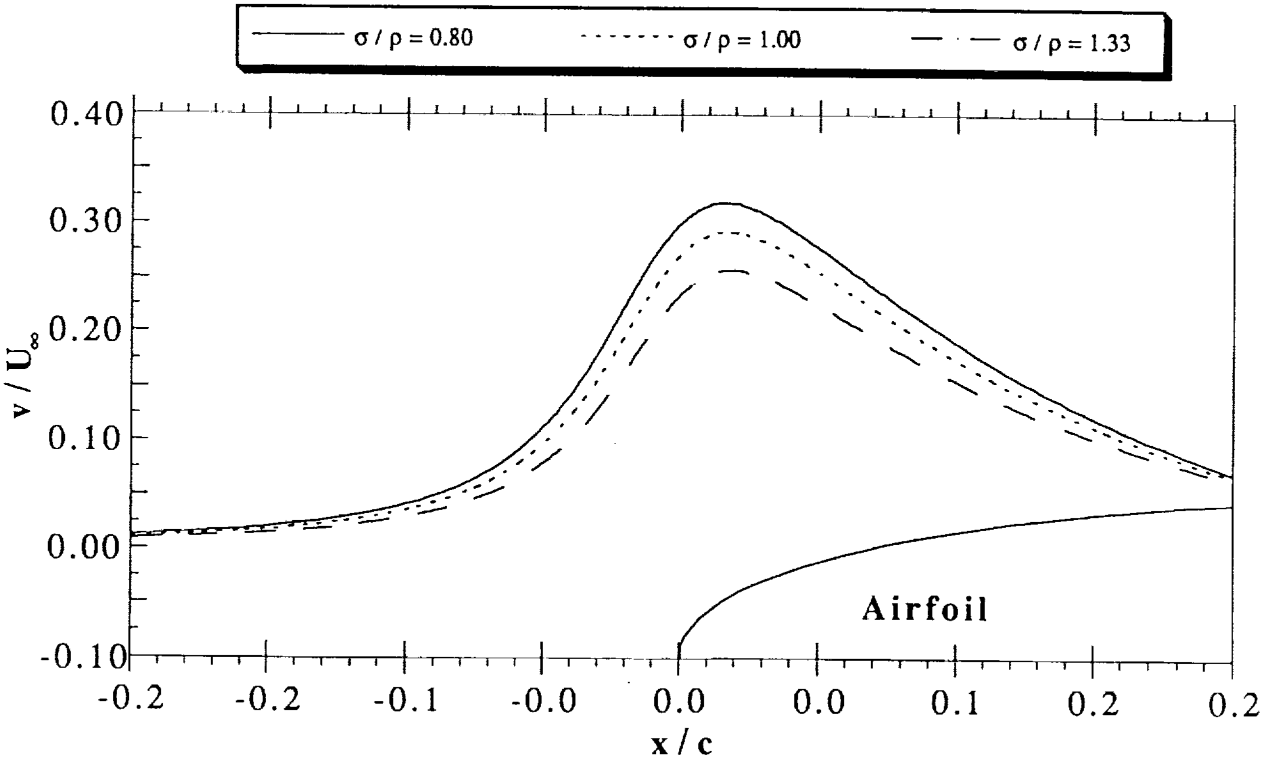

Fig. 4: The effect of density ratio on v/U∞ for a computational bubble trajectory for a bubble diameter of 3.0mm.

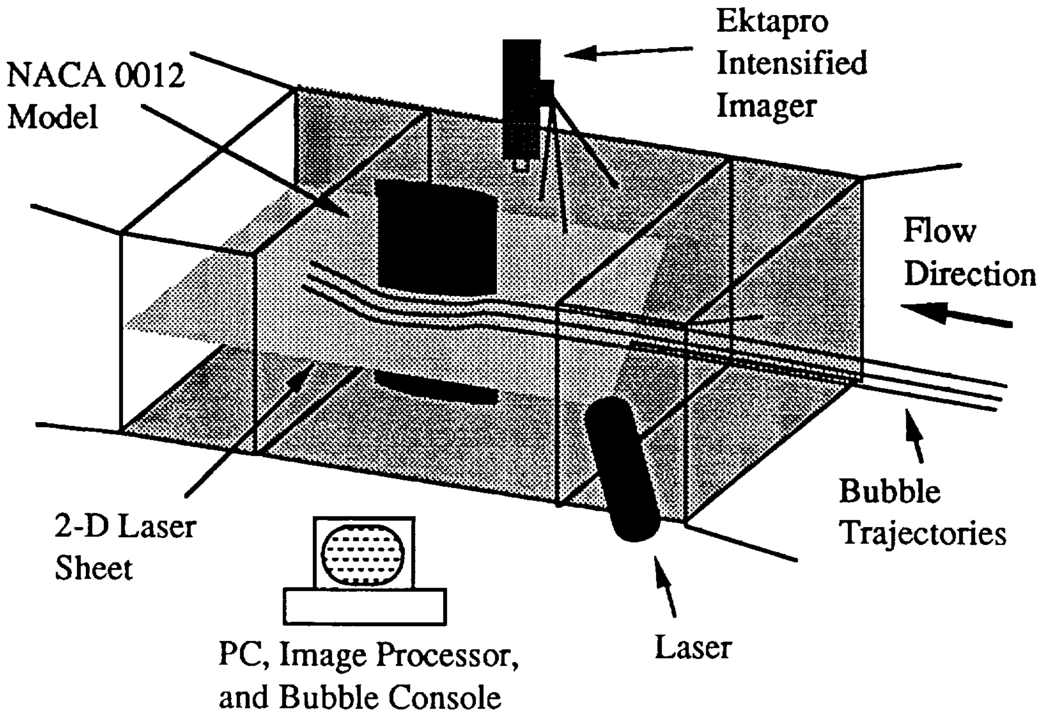

Fig. 5: 2-D experimental test section set-up schematic

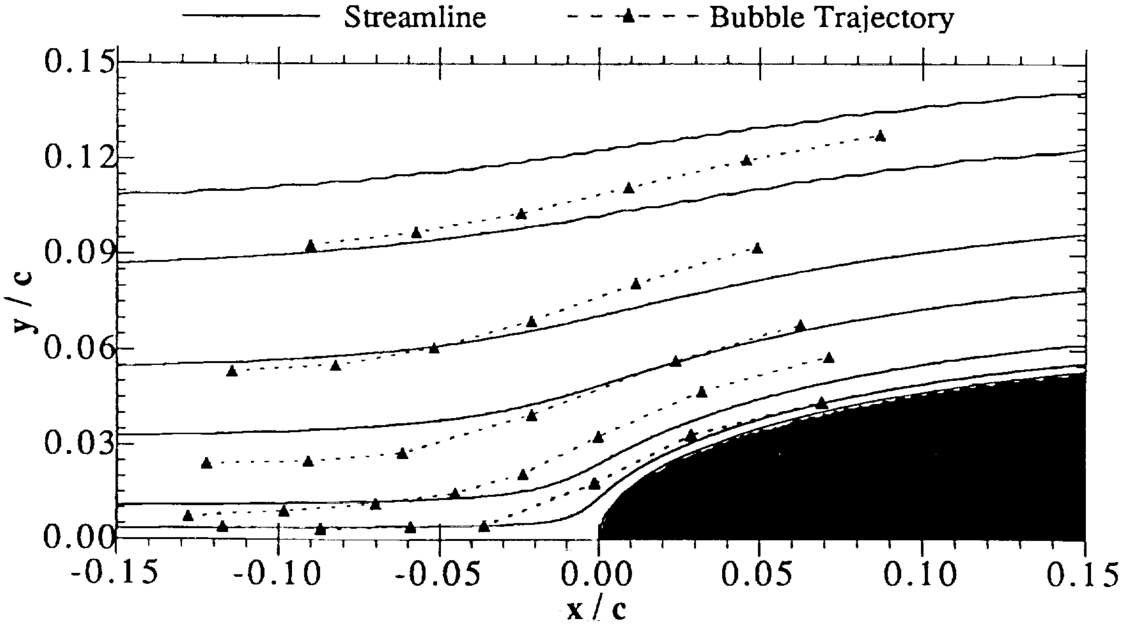

Fig. 6: Experimental bubble trajectories versus flow-field streamlines.

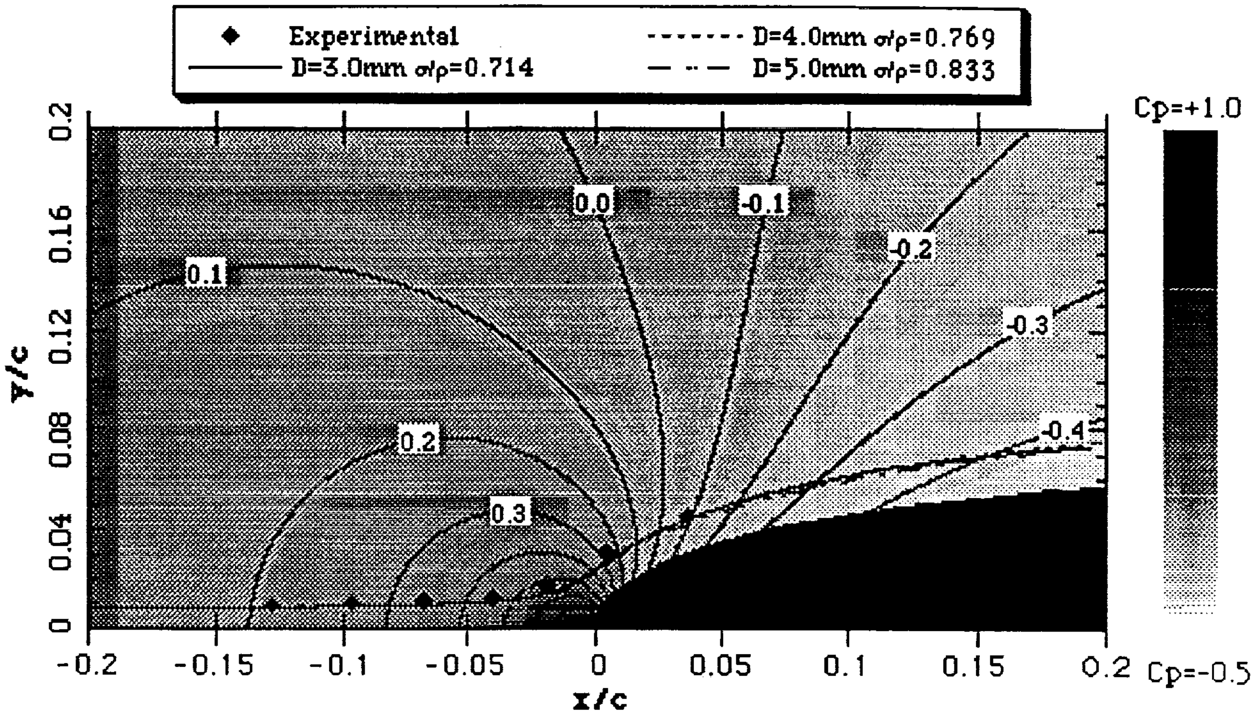

Fig. 7: Comparison of experimental and computational bubble trajectories for bubble #24.

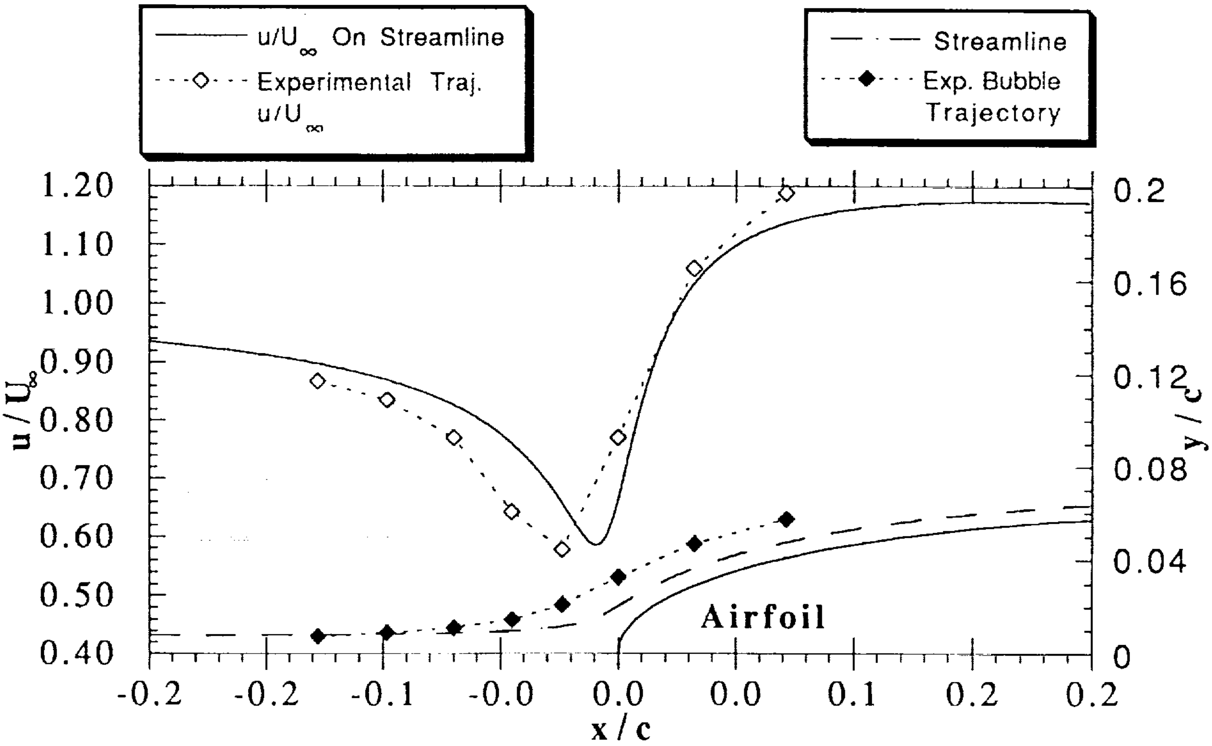

Fig. 8: Comparison of the streamwise component of velocity for experimental trajectory #33 to the streamwise velocity at points along a streamline.

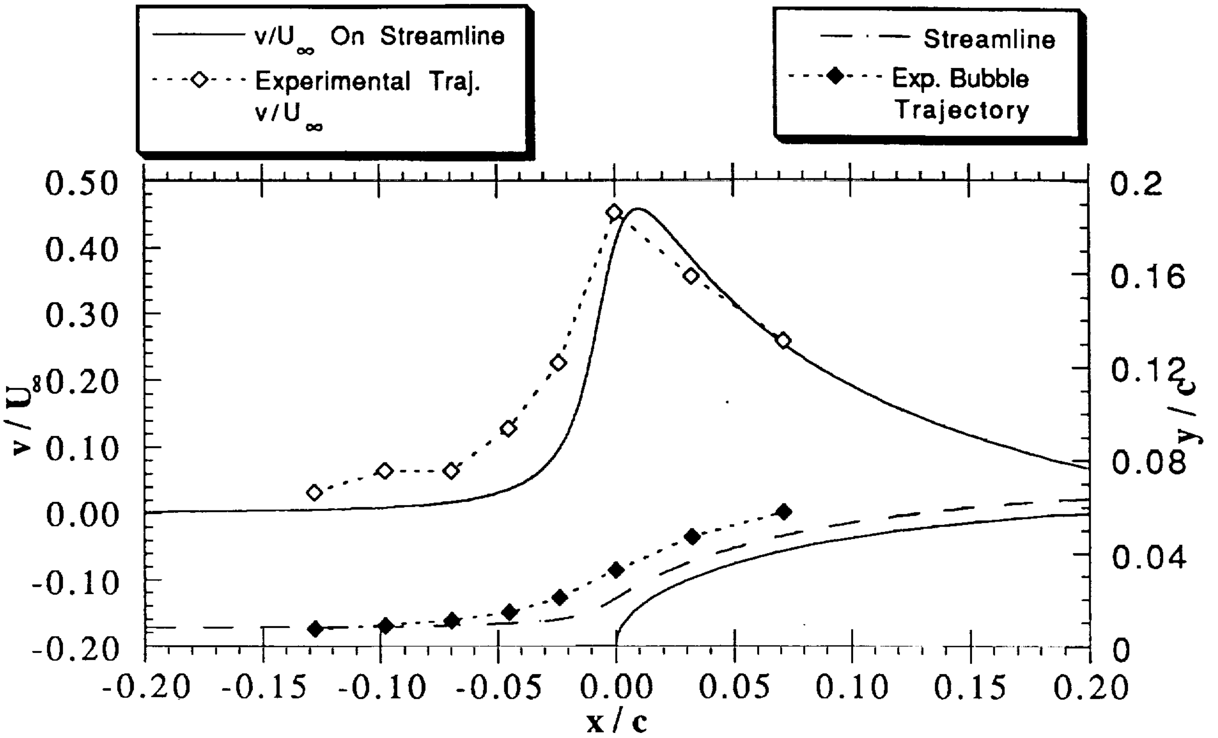

Fig. 9: Comparison of the normal component of velocity for experimental trajectory #33 to the normal velocity at points along a streamline.

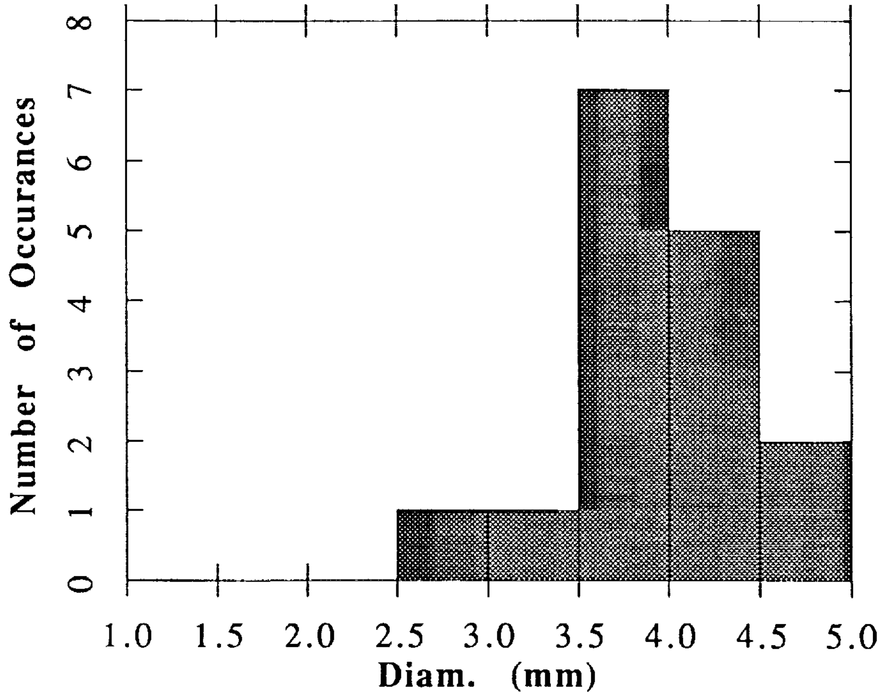

Fig. 10: Histogram of the estimated bubble diameters obtained from the computational trajectories.

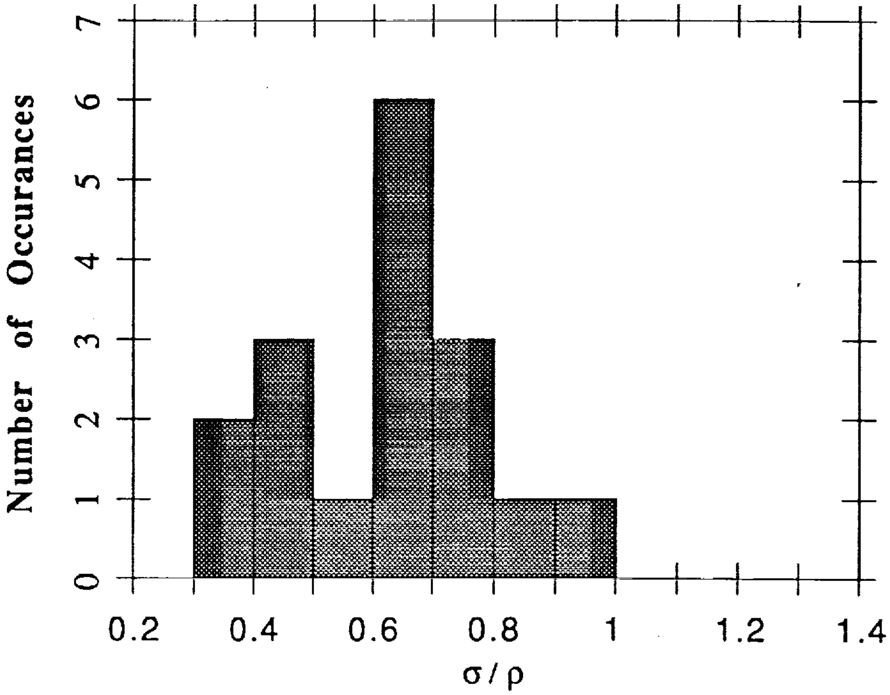

Fig. 11: Histogram of the estimated bubble density ratios obtained from the computational trajectories.

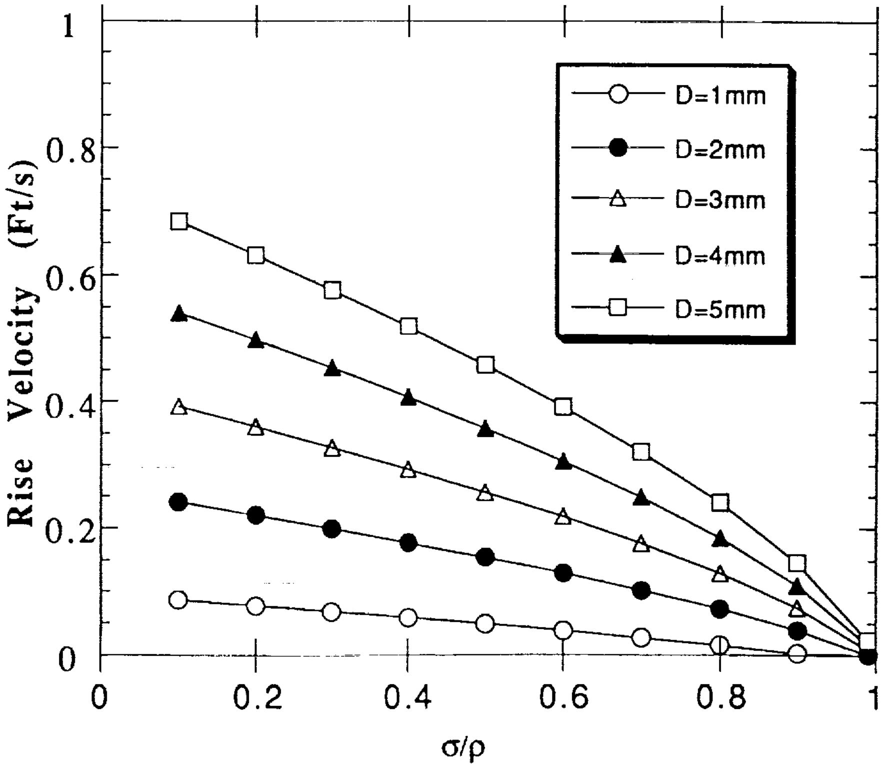

Fig. 12: Bubble rise velocity versus density ratio.

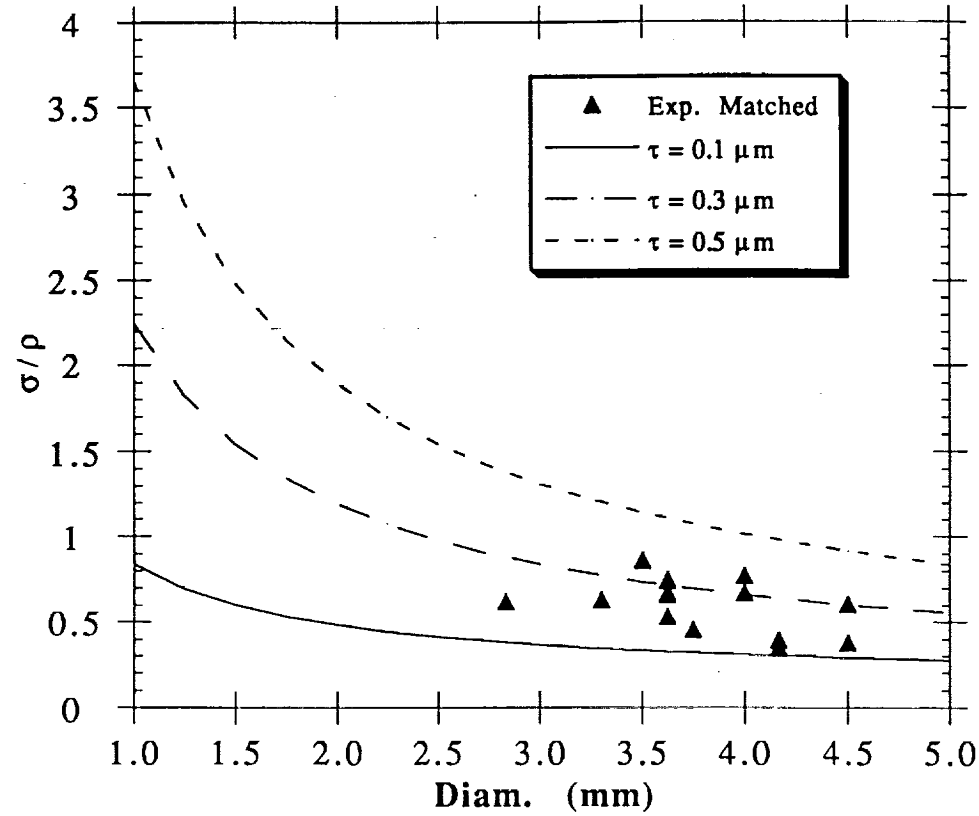

Fig. 13: Comparison of estimated diameter versus density ratio to wall thickness.

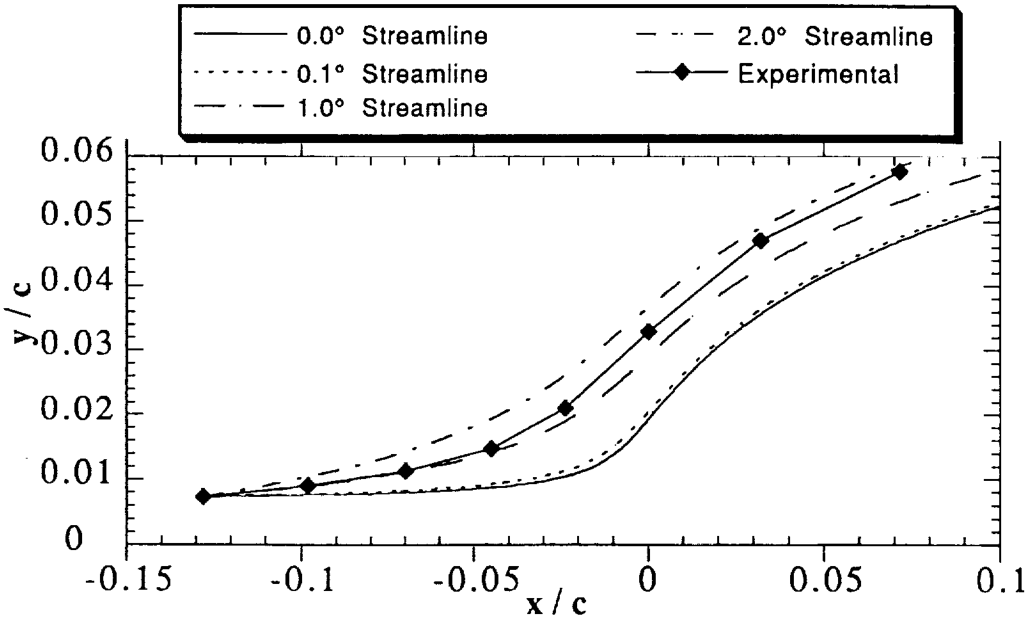

Fig. 14: Comparison of several streamlines generated for different angles of attack to an experimental trajectory.

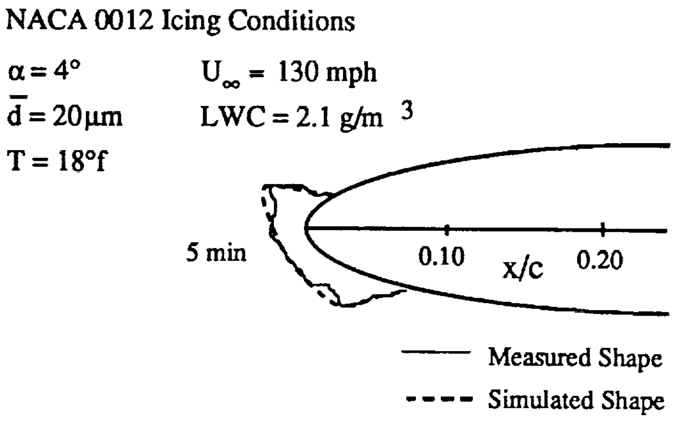

Fig. 15: Simulated glaze ice accretion

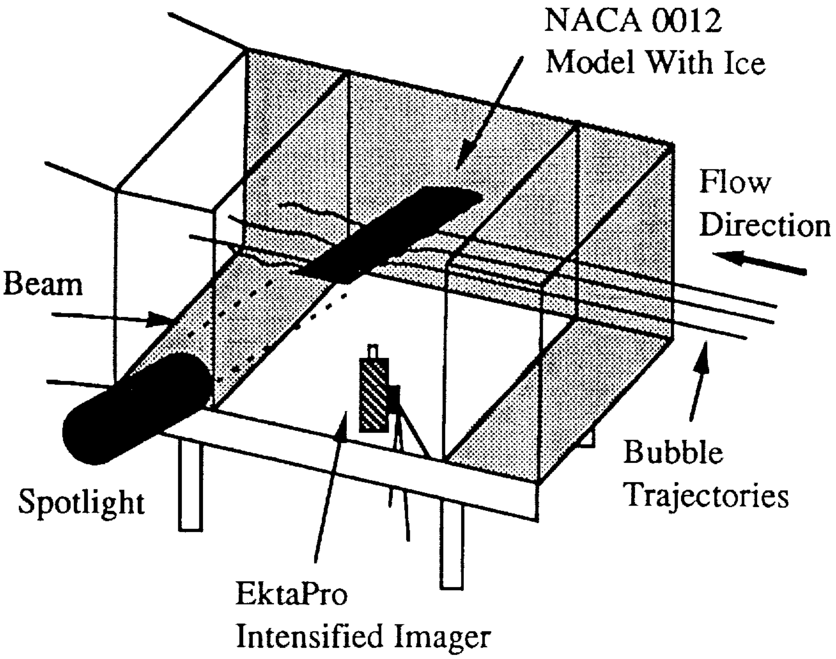

Fig. 16: Tunnel set-up for the 3-D test.

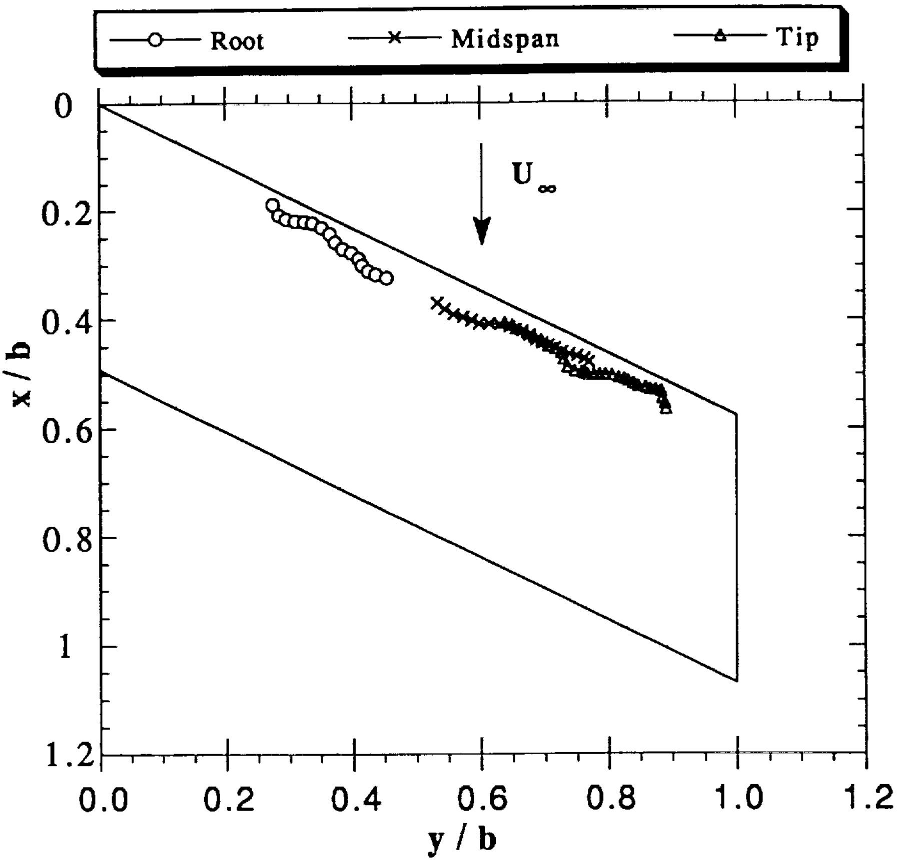

Fig. 17: Single bubble trajectories for the root, midspan, and tip stations for the iced model at 4° and Re=6.5×10^5.

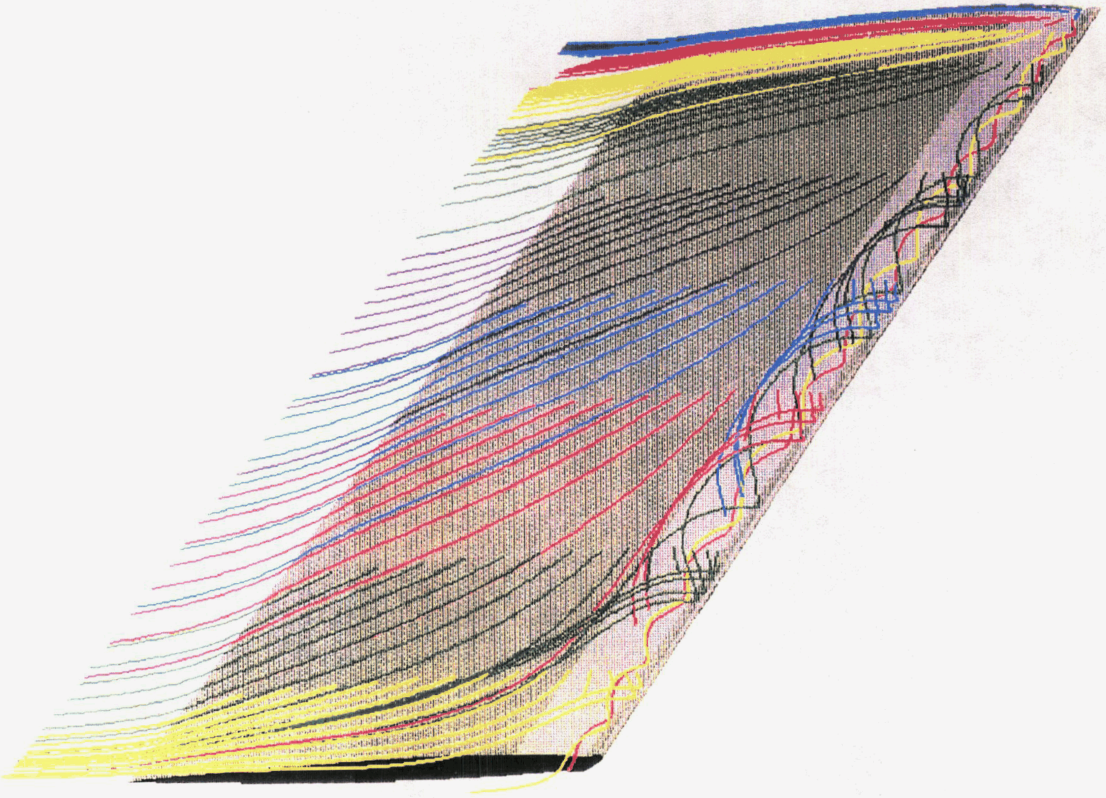

Fig. 18: Navier-Stokes simulation of the NACA 0012 semispan wing with simulated glaze ice at 4° angle of attack and Re=1.5×10^6 [24]

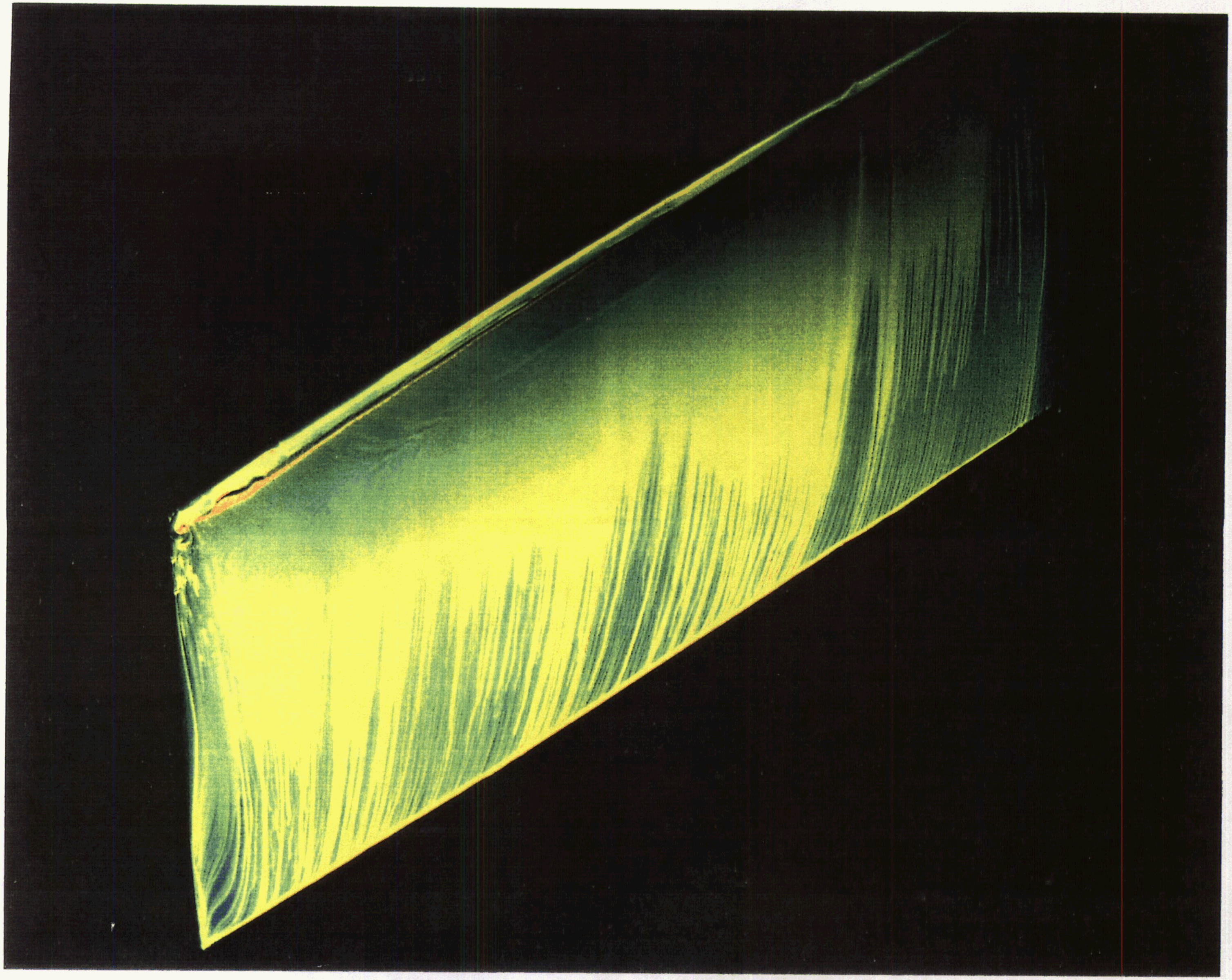

Fig. 19: Surface oil flow visualization of the NACA 0012 semispan wing with simulated glaze ice at 4° angle of attack and $Re=1.2x10^6$

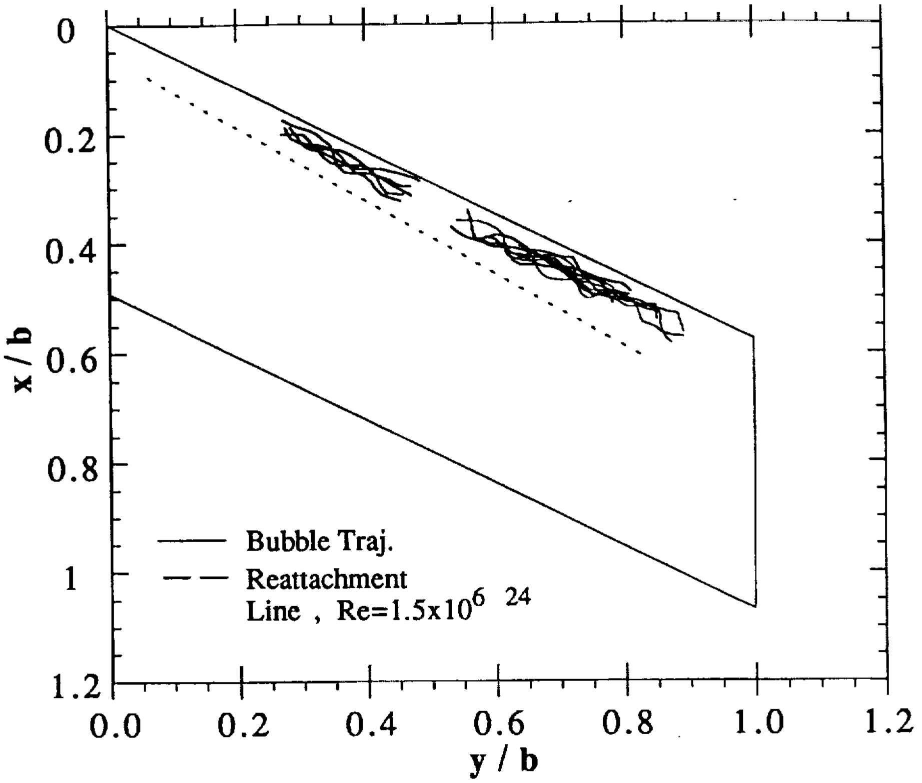

Fig. 20: Bubble trajectories for the iced model at 4° angle of attack and Re=6.5×10^5.

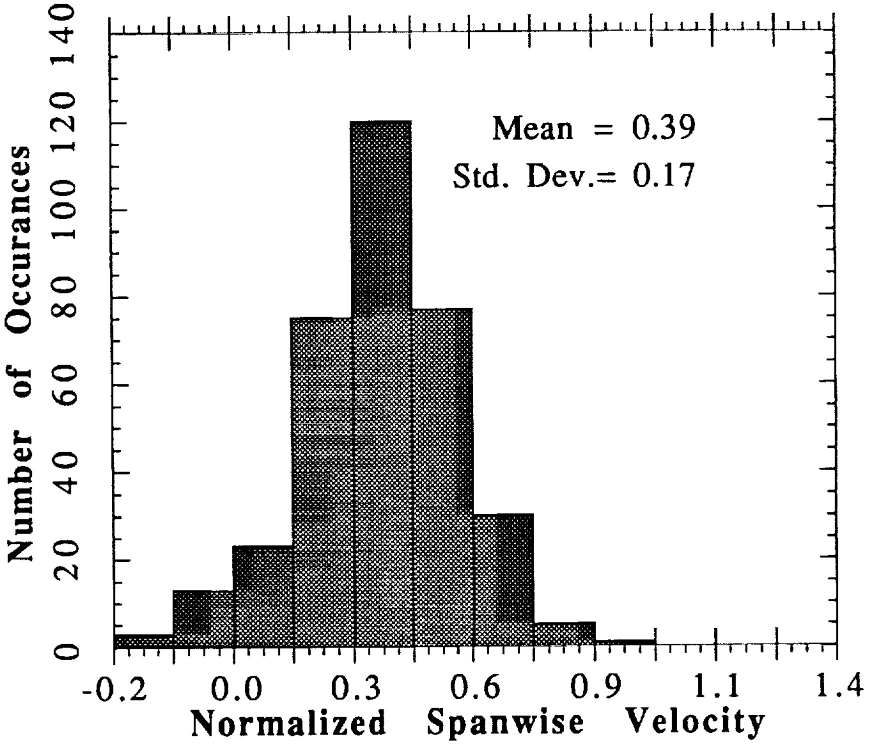

Fig. 21: Histogram of the normalized spanwise velocity in the separated region for 4° angle of attack and Re=6.5×10^5.

PRECEDING PAGE BLANK NOT FILMED

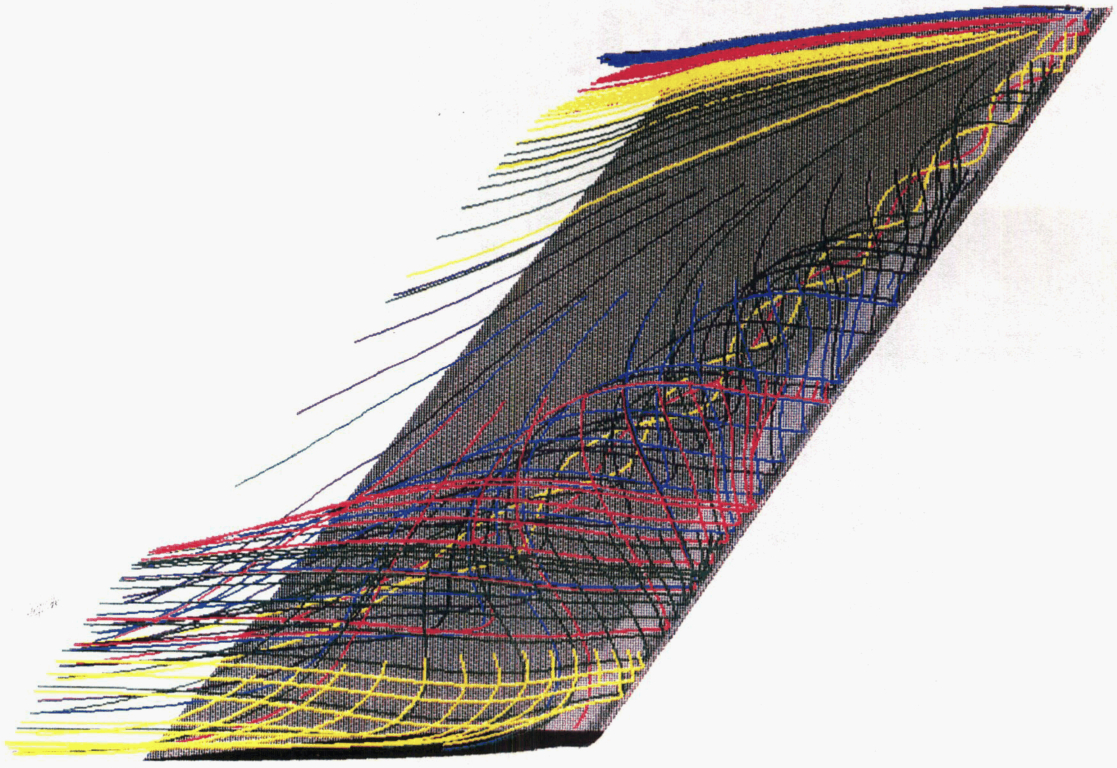

Fig. 22: Navier-Stokes simulation of the NACA 0012 semispan wing with simulated glaze ice at 8° angle of attack and $Re=1.5x10^6$ [24]

Fig. 23: Surface oil flow visualization of the NACA 0012 semispan wing with simulated glaze ice at 8° angle of attack and $Re=1.2x10^6$

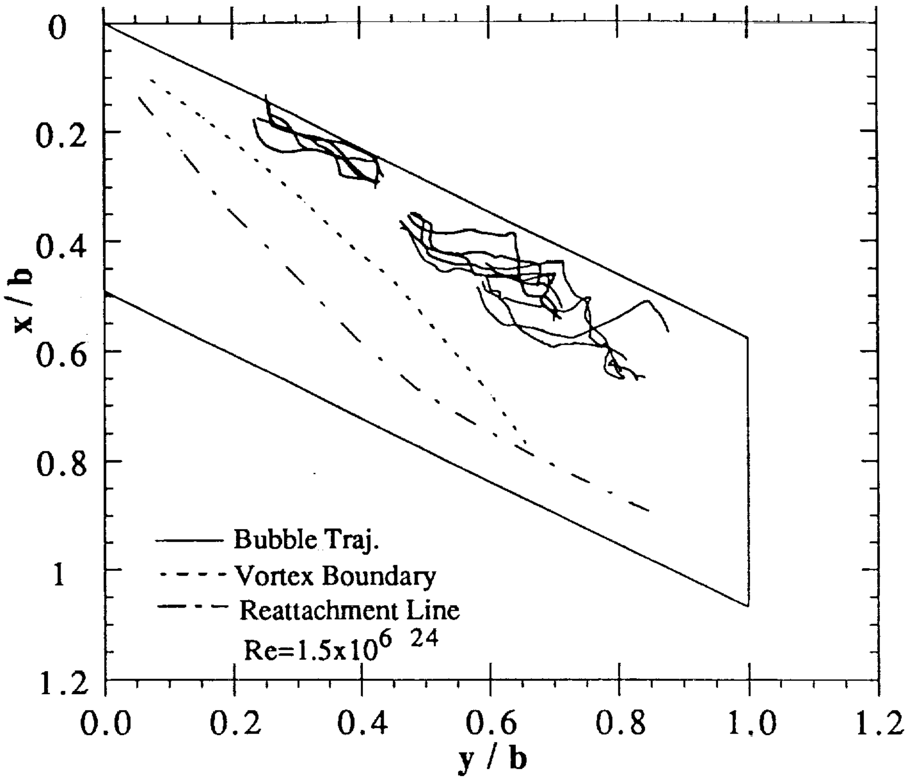

Fig. 24: Bubble trajectories for the iced model at 8° angle of attack and $Re=6.5x10^5$.

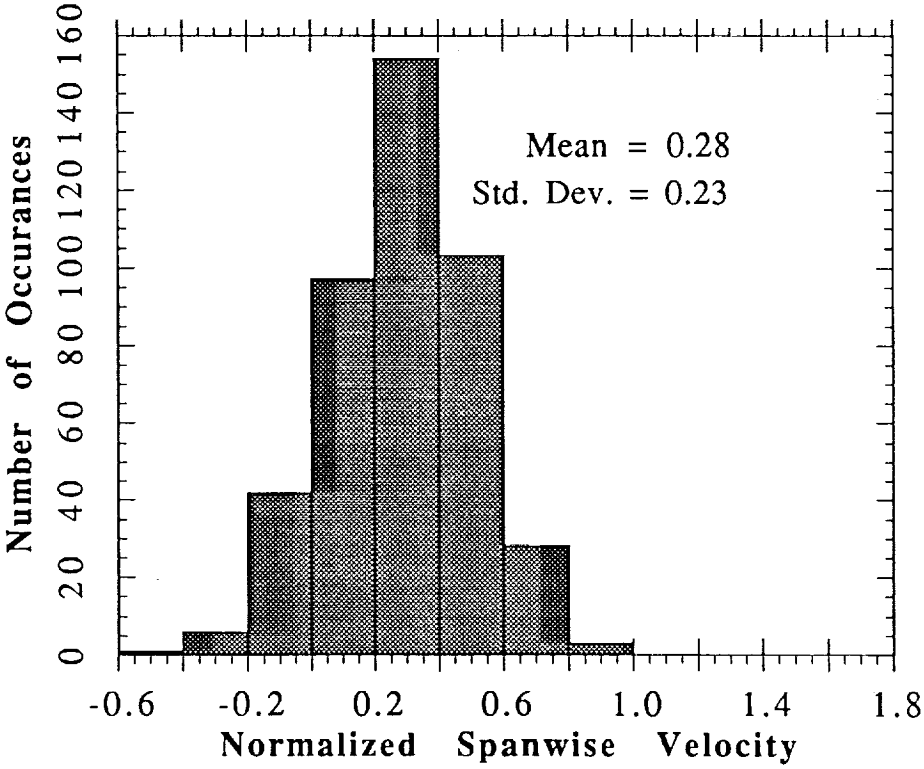

Fig. 25: Histogram of the normalized spanwise velocity in the separated region for 8° angle of attack and $Re=6.5x10^5$.

APPENDIX A

2-D Experimental Data:

Bubble #1:

x/c	y/c	u/U_∞*	v/U_∞*
-0.09600	0.03470		
-0.06613	0.03709	0.85740	0.06869
-0.03733	0.04187	0.82678	0.13738
-0.00960	0.04905	0.79615	0.20607
0.02133	0.06341	0.88802	0.41214
0.06080	0.07178	1.13299	0.24042

Bubble #2:

x/c	y/c	u/U_∞*	v/U_∞*
-0.08960	0.12921		
-0.05547	0.13041	0.97988	0.03435
-0.02240	0.13400	0.94926	0.10304
0.01280	0.13998	1.01050	0.17173
0.04907	0.14476	1.04113	0.13738
0.08960	0.15074	1.16361	0.17173

Bubble #3:

x/c	y/c	u/U_∞*	v/U_∞*
-0.10560	0.01196		
-0.07573	0.01196	0.85740	0.00000
-0.04907	0.01077	0.76553	-0.03435
-0.02560	0.01196	0.67367	0.03435
-0.00853	0.02034	0.48994	0.24042
0.01493	0.03828	0.67367	0.51518
0.05013	0.05025	1.01050	0.34345

---

* u/U_∞ and v/U_∞ were calculated by finite difference one-half way between the measured particle locations. For example, from bubble #1, the values u/U_∞=0.85740 and v/U_∞=0.06869 are calculated to be the bubble velocity at x/c=-0.08107 and y/c=0.03589. All u/U_∞ and v/U_∞ values tabulated in APPENDIX A should be interpreted in this manner.

Bubble #5:

x/c	y/c	$u/U_\infty{}^*$	$v/U_\infty{}^*$
-0.07893	0.06102		
-0.05013	0.06580	0.82678	0.13738
-0.02133	0.07178	0.82678	0.17173
0.01067	0.08135	0.91864	0.27476
0.04480	0.08973	0.97988	0.24042
0.08427	0.09571	1.13299	0.17173

Bubble #5.5:

x/c	y/c	$u/U_\infty{}^*$	$v/U_\infty{}^*$
-0.07893	0.06341		
-0.04800	0.06700	0.88802	0.10304
-0.01813	0.07418	0.85740	0.20607
0.01493	0.08375	0.94926	0.27476
0.05227	0.09332	1.07175	0.27476
0.09280	0.10050	1.16361	0.20607

Bubble #6:

x/c	y/c	$u/U_\infty{}^*$	$v/U_\infty{}^*$
-0.09493	0.01795		
-0.06507	0.01795	0.85740	0.00000
-0.03947	0.01795	0.73491	0.00000
-0.01813	0.02393	0.61243	0.17173
0.00533	0.03589	0.67367	0.34345
0.03947	0.05144	0.97988	0.44649
0.07787	0.06341	1.10237	0.34345

Bubble #8:

x/c	y/c	$u/U_\infty{}^*$	$v/U_\infty{}^*$
-0.10987	0.03111		
-0.07787	0.03470	0.91864	0.10304
-0.05120	0.03948	0.76553	0.13738
-0.02560	0.04786	0.73491	0.24042
0.00320	0.06102	0.82678	0.37780
0.04053	0.07418	1.07175	0.37780
0.08107	0.08135	1.16361	0.20607

Bubble #10:

x/c	y/c	u/U_{∞}^{*}	v/U_{∞}^{*}
-0.08640	0.06221		
-0.05653	0.06580	0.85740	0.10304
-0.02667	0.07059	0.85740	0.13738
0.00427	0.08016	0.88802	0.27476
0.03947	0.08853	1.01050	0.24042
0.07893	0.09810	1.13299	0.27476

Bubble #12:

x/c	y/c	u/U_{∞}^{*}	v/U_{∞}^{*}
-0.11555	0.04711		
-0.08333	0.04845	0.92025	0.03844
-0.05333	0.05384	0.85679	0.15376
-0.02333	0.06057	0.85679	0.19220
0.00778	0.07268	0.88852	0.34596
0.04444	0.08345	1.04718	0.30752
0.08555	0.09287	1.17411	0.26908

Bubble #14:

x/c	y/c	u/U_{∞}^{*}	v/U_{∞}^{*}
-0.10667	0.09152		
-0.07333	0.09422	0.95198	0.07688
-0.04111	0.09960	0.92025	0.15376
-0.00778	0.10633	0.95198	0.19220
0.02667	0.11575	0.98372	0.26908
0.06555	0.12383	1.11065	0.23064
0.10889	0.13190	1.23758	0.23064

Bubble #15:

x/c	y/c	u/U_{∞}^{*}	v/U_{∞}^{*}
-0.13111	0.05249		
-0.09778	0.05384	0.95198	0.03844
-0.06667	0.05653	0.88852	0.07688
-0.03667	0.06460	0.85679	0.23064
-0.00556	0.07403	0.88852	0.26908
0.02889	0.08749	0.98372	0.38440
0.07000	0.09691	1.17411	0.26908

Bubble #16:

x/c	y/c	$u/U_\infty{}^*$	$v/U_\infty{}^*$
-0.13889	0.02423		
-0.10555	0.02423	0.95198	0.00000
-0.07555	0.02557	0.85679	0.03844
-0.04778	0.02961	0.79332	0.11532
0.00556	0.04980	1.52317	0.57660
0.04222	0.06326	1.04718	0.38440
0.08333	0.07268	1.17411	0.26908

Bubble #18:

x/c	y/c	$u/U_\infty{}^*$	$v/U_\infty{}^*$
-0.13972	0.05587		
-0.10592	0.05820	0.95374	0.06569
-0.07324	0.06286	0.92195	0.13137
-0.04282	0.06868	0.85837	0.16422
-0.01127	0.07799	0.89016	0.26275
0.02479	0.08963	1.01733	0.32844
0.06535	0.09778	1.14449	0.22991
0.11155	0.10709	1.30345	0.26275

Bubble #21:

x/c	y/c	$u/U_\infty{}^*$	$v/U_\infty{}^*$
-0.08563	0.01746		
-0.05859	0.01746	0.76299	0.00000
-0.03380	0.02212	0.69941	0.13137
-0.01127	0.03143	0.63583	0.26275
0.01915	0.04773	0.85837	0.45981
0.05859	0.05937	1.11270	0.32844
0.10253	0.06868	1.23987	0.26275

Bubble #24:

x/c	y/c	$u/U_\infty{}^*$	$v/U_\infty{}^*$
-0.14422	0.00793		
-0.11042	0.00907	0.96359	0.03231
-0.08000	0.01020	0.86723	0.03231
-0.05183	0.01133	0.80300	0.03231
-0.02817	0.01360	0.67452	0.06461
-0.00789	0.02153	0.57816	0.22615
0.01803	0.03740	0.73876	0.45230
0.05521	0.05100	1.05995	0.38769

Bubble #28:

x/c	y/c	u/U_{∞}^{*}	v/U_{∞}^{*}
-0.09465	0.00567		
-0.06648	0.00680	0.80300	0.03231
-0.04282	0.00793	0.67452	0.03231
-0.02366	0.01360	0.54604	0.16154
-0.00451	0.02607	0.54604	0.35538
0.02817	0.04307	0.93147	0.48461
0.06873	0.05440	1.15631	0.32307
0.11268	0.06120	1.25267	0.19384

Bubble #30:

x/c	y/c	u/U_{∞}^{*}	v/U_{∞}^{*}
-0.13296	0.00453		
-0.10141	0.00340	0.89935	-0.03231
-0.07211	0.00340	0.83512	0.00000
-0.04620	0.00453	0.73876	0.03231
-0.02592	0.00453	0.57816	0.00000
-0.01127	0.00907	0.41756	0.12923
0.00901	0.02720	0.57816	0.51692
0.04845	0.03967	1.12419	0.35538
0.09014	0.04760	1.18843	0.22615

Bubble #33:

x/c	y/c	u/U_{∞}^{*}	v/U_{∞}^{*}
-0.14310	0.00680		
-0.11268	0.00793	0.86723	0.03231
-0.08338	0.01020	0.83512	0.06461
-0.05634	0.01247	0.77088	0.06461
-0.03380	0.01700	0.64240	0.12923
-0.01352	0.02493	0.57816	0.22615
0.01352	0.04080	0.77088	0.45230
0.05070	0.05327	1.05995	0.35538
0.09239	0.06233	1.18843	0.25846

Bubble #35:

x/c	y/c	$u/U_\infty{}^*$	$v/U_\infty{}^*$
-0.11413	0.01133		
-0.08320	0.01247	0.88127	0.03229
-0.05547	0.01247	0.79010	0.00000
-0.03093	0.01473	0.69893	0.06458
-0.01067	0.02153	0.57738	0.19374
0.01280	0.03740	0.66855	0.45206
0.04907	0.04987	1.03321	0.35519
0.09067	0.05780	1.18515	0.22603

APPENDIX B

Computational Trajectories versus 2-D Data:

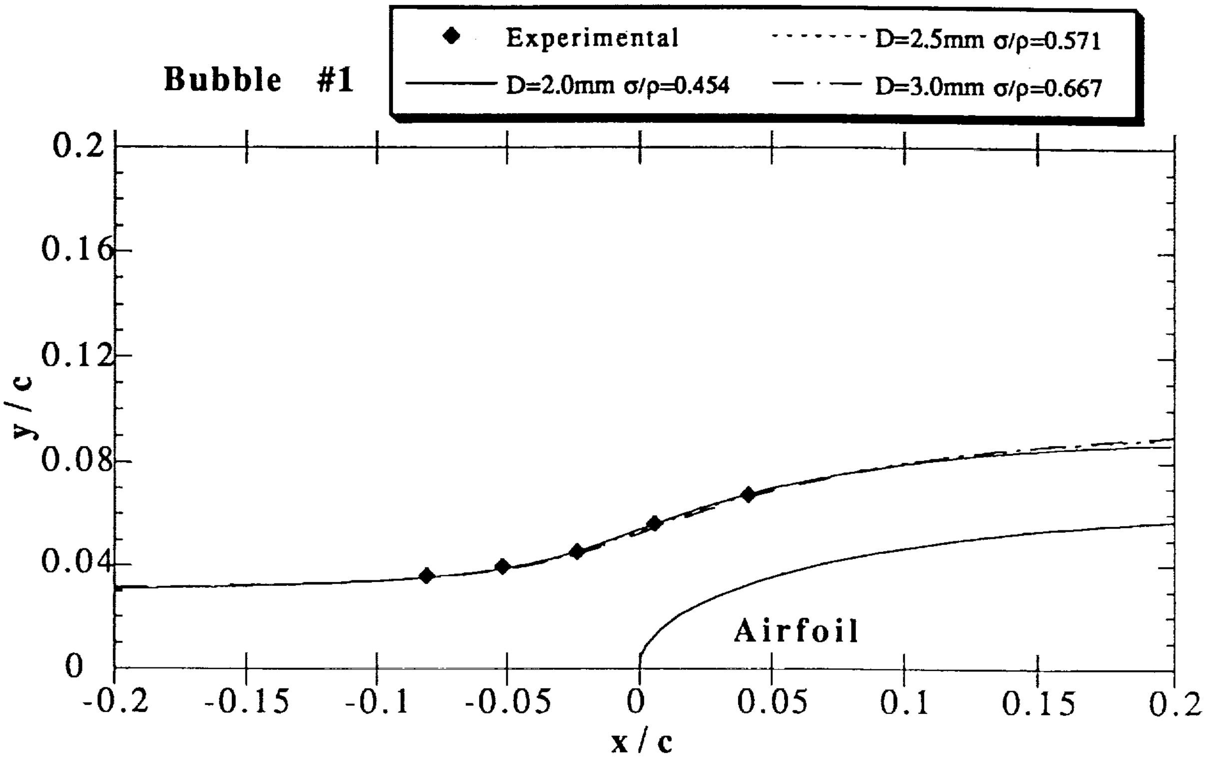

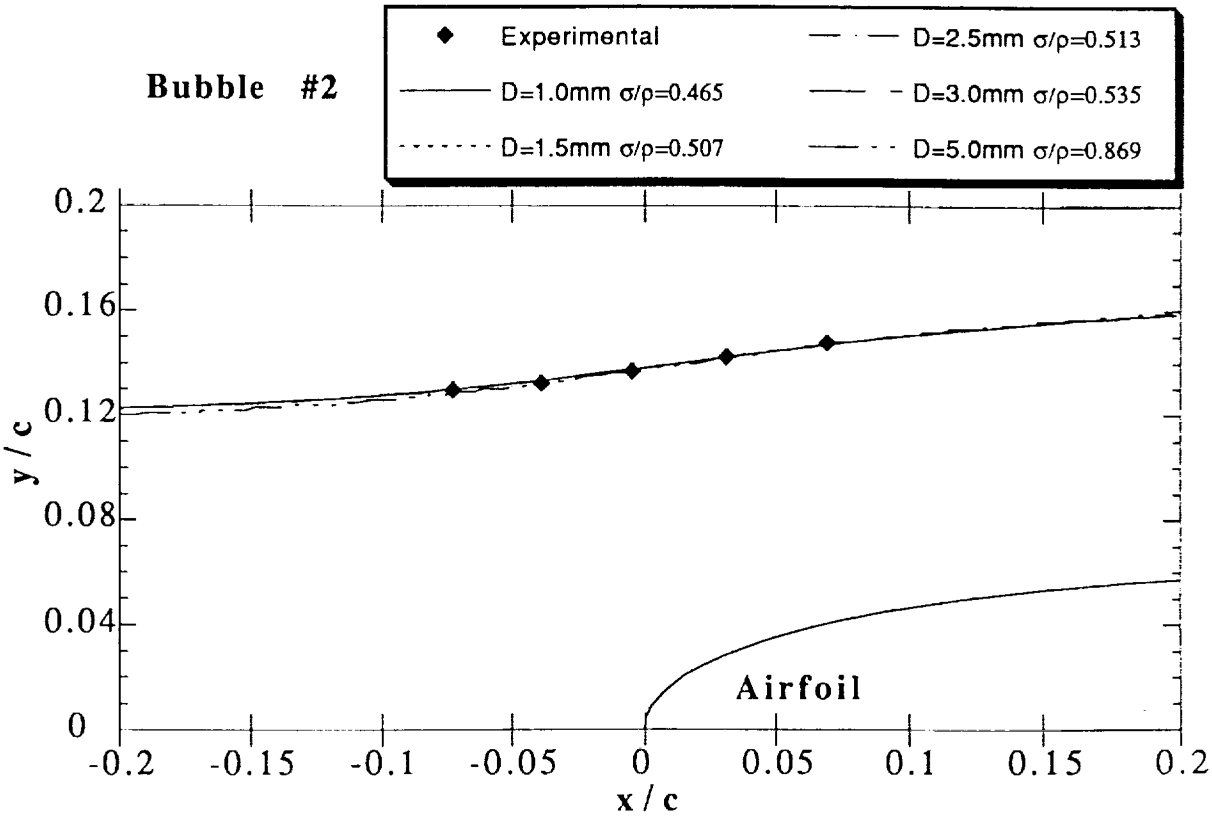

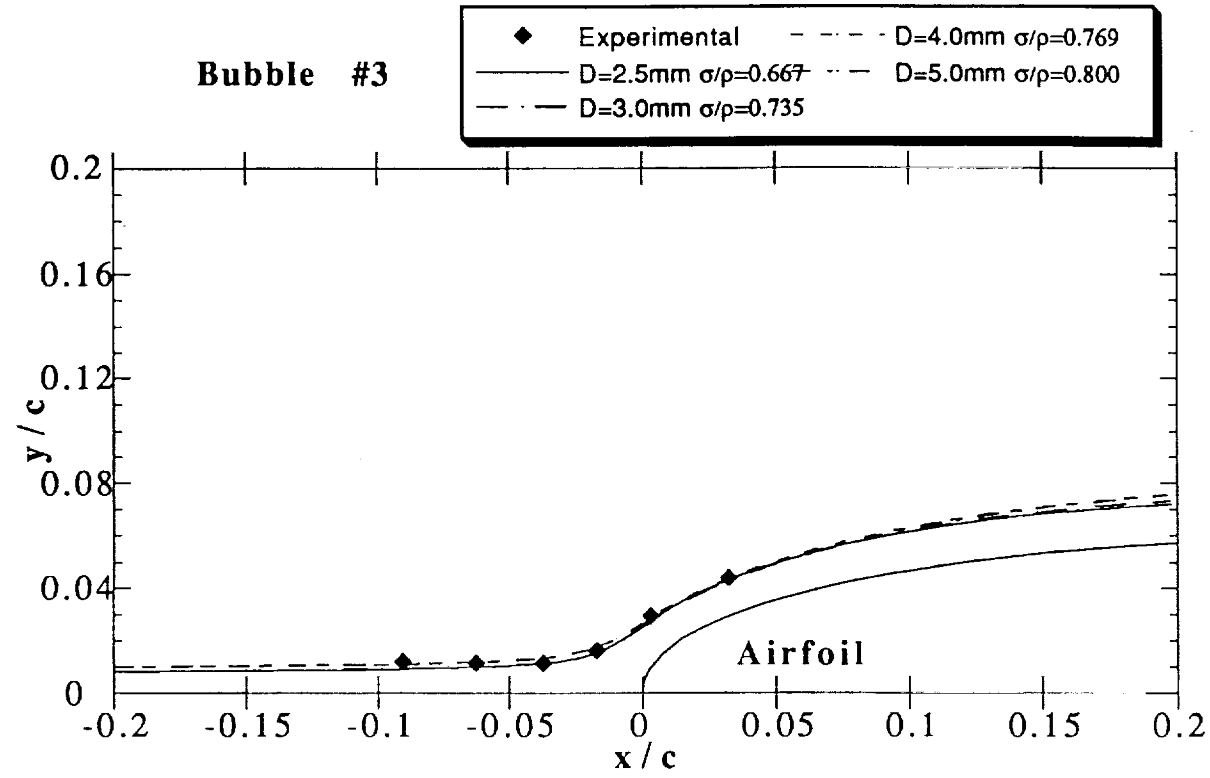

Bubble #3

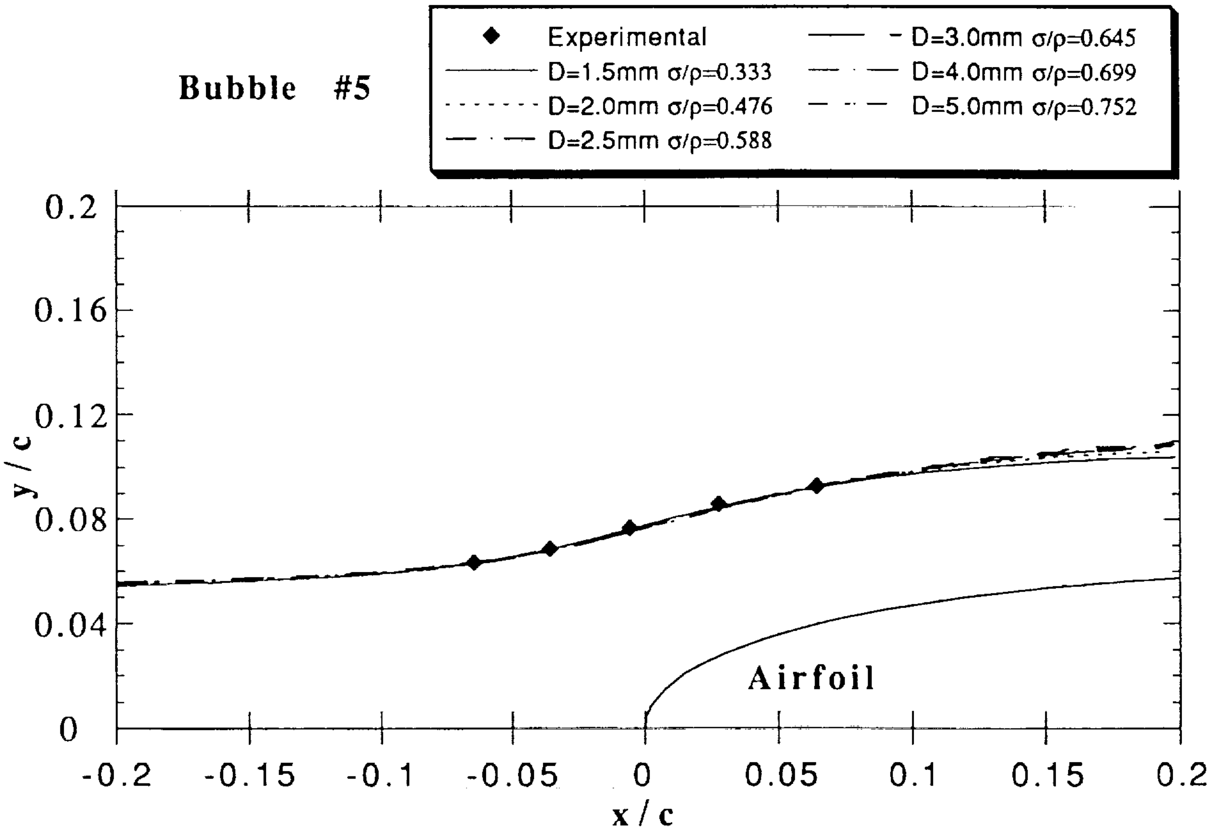

Bubble #5

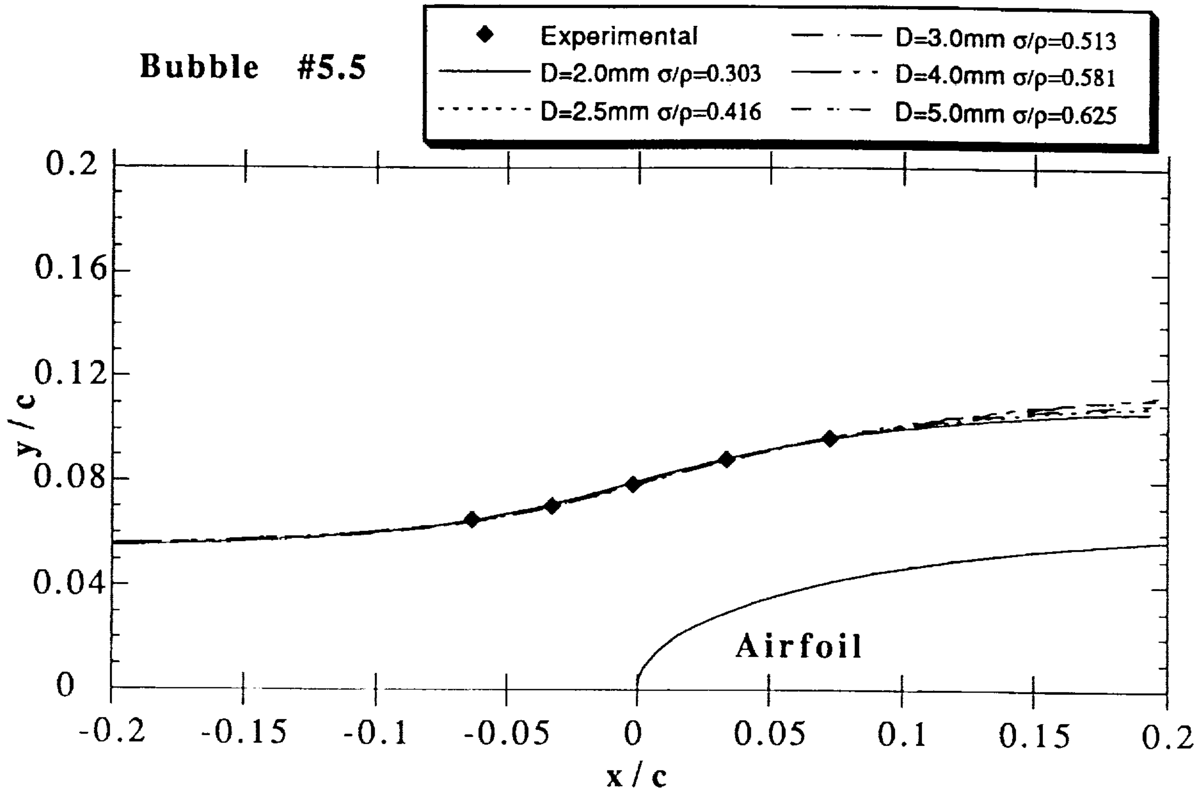
Bubble #5.5
◆ Experimental
D=2.0mm σ/ρ=0.303
D=2.5mm σ/ρ=0.416
D=3.0mm σ/ρ=0.513
D=4.0mm σ/ρ=0.581
D=5.0mm σ/ρ=0.625
0.2
0.16
0.12
0.08
0.04
0
y / c
-0.2
-0.15
-0.1
-0.05
0
0.05
0.1
0.15
0.2
x / c
Airfoil

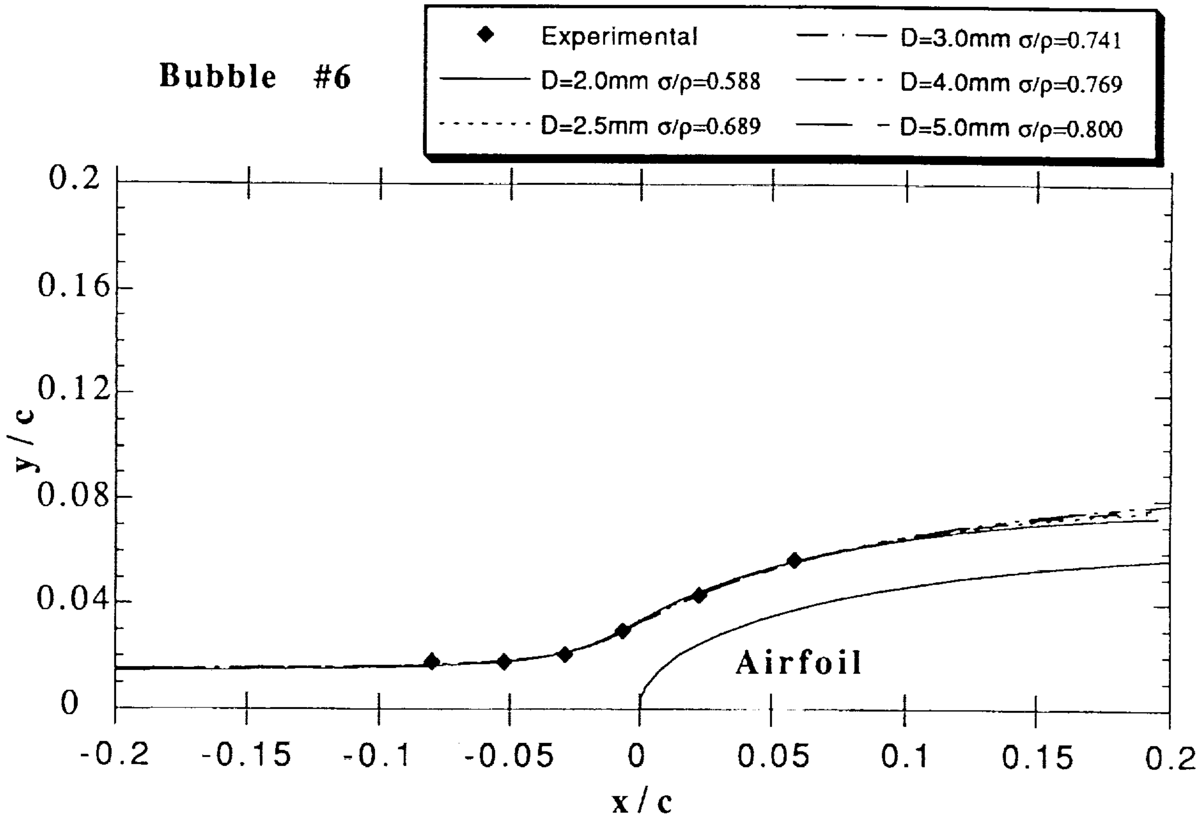
Bubble #6
◆ Experimental
D=2.0mm σ/ρ=0.588
D=2.5mm σ/ρ=0.689
D=3.0mm σ/ρ=0.741
D=4.0mm σ/ρ=0.769
D=5.0mm σ/ρ=0.800
0.2
0.16
0.12
0.08
0.04
0
y / c
-0.2
-0.15
-0.1
-0.05
0
0.05
0.1
0.15
0.2
x / c
Airfoil

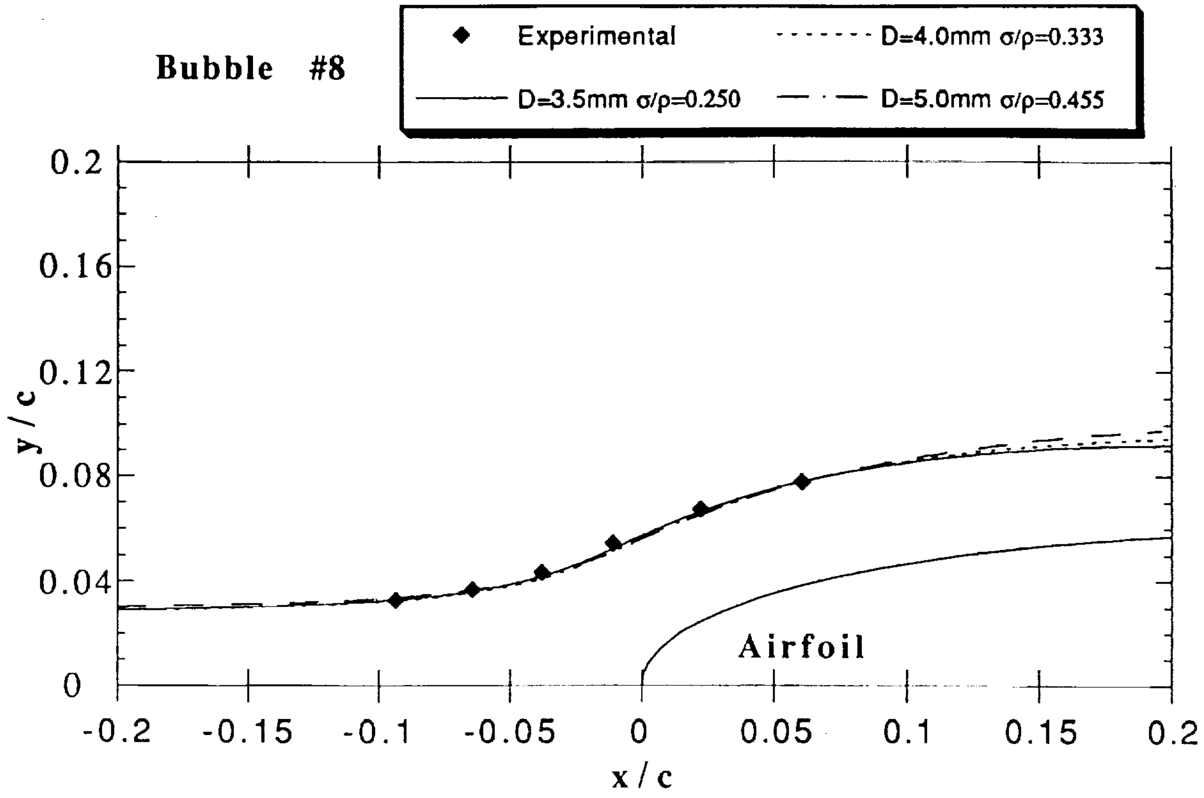
Bubble #8
Experimental
D=4.0mm σ/ρ=0.333
D=3.5mm σ/ρ=0.250
D=5.0mm σ/ρ=0.455
y / c
0.2
0.16
0.12
0.08
0.04
0
Airfoil
-0.2
-0.15
-0.1
-0.05
0
0.05
0.1
0.15
0.2
x / c

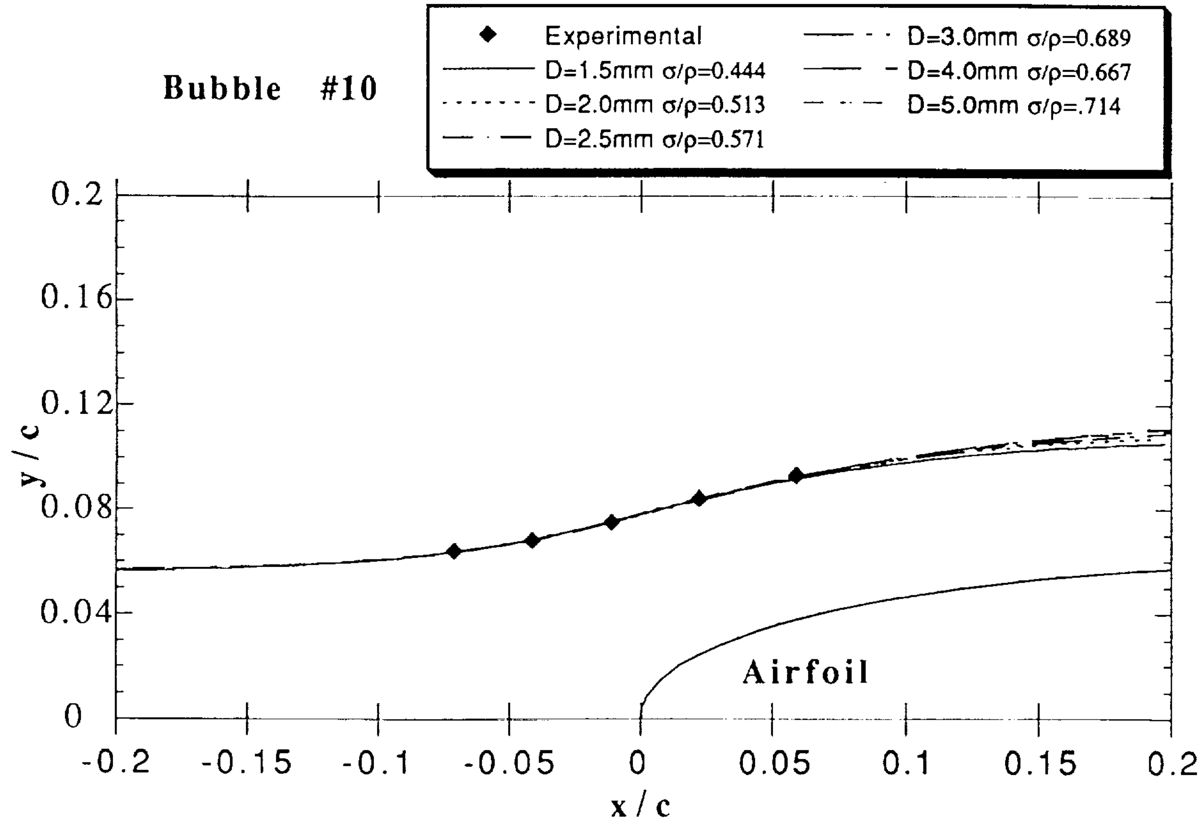
Bubble #10
Experimental
D=3.0mm σ/ρ=0.689
D=1.5mm σ/ρ=0.444
D=4.0mm σ/ρ=0.667
D=2.0mm σ/ρ=0.513
D=5.0mm σ/ρ=.714
D=2.5mm σ/ρ=0.571
y / c
0.2
0.16
0.12
0.08
0.04
0
Airfoil
-0.2
-0.15
-0.1
-0.05
0
0.05
0.1
0.15
0.2
x / c

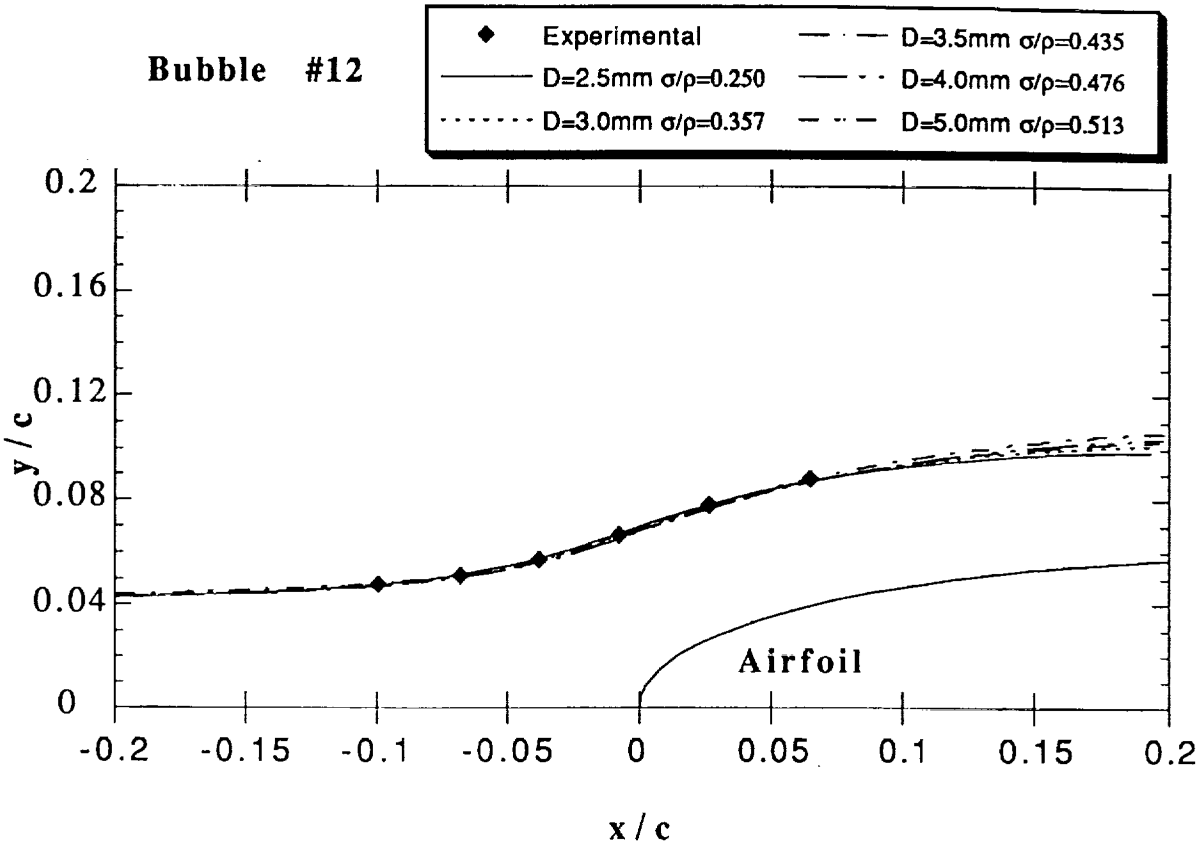
Bubble #12
◆ Experimental
D=2.5mm σ/ρ=0.250
D=3.0mm σ/ρ=0.357
D=3.5mm σ/ρ=0.435
D=4.0mm σ/ρ=0.476
D=5.0mm σ/ρ=0.513
y / c
0.2
0.16
0.12
0.08
0.04
0
-0.2
-0.15
-0.1
-0.05
0
0.05
0.1
0.15
0.2
x / c
Airfoil

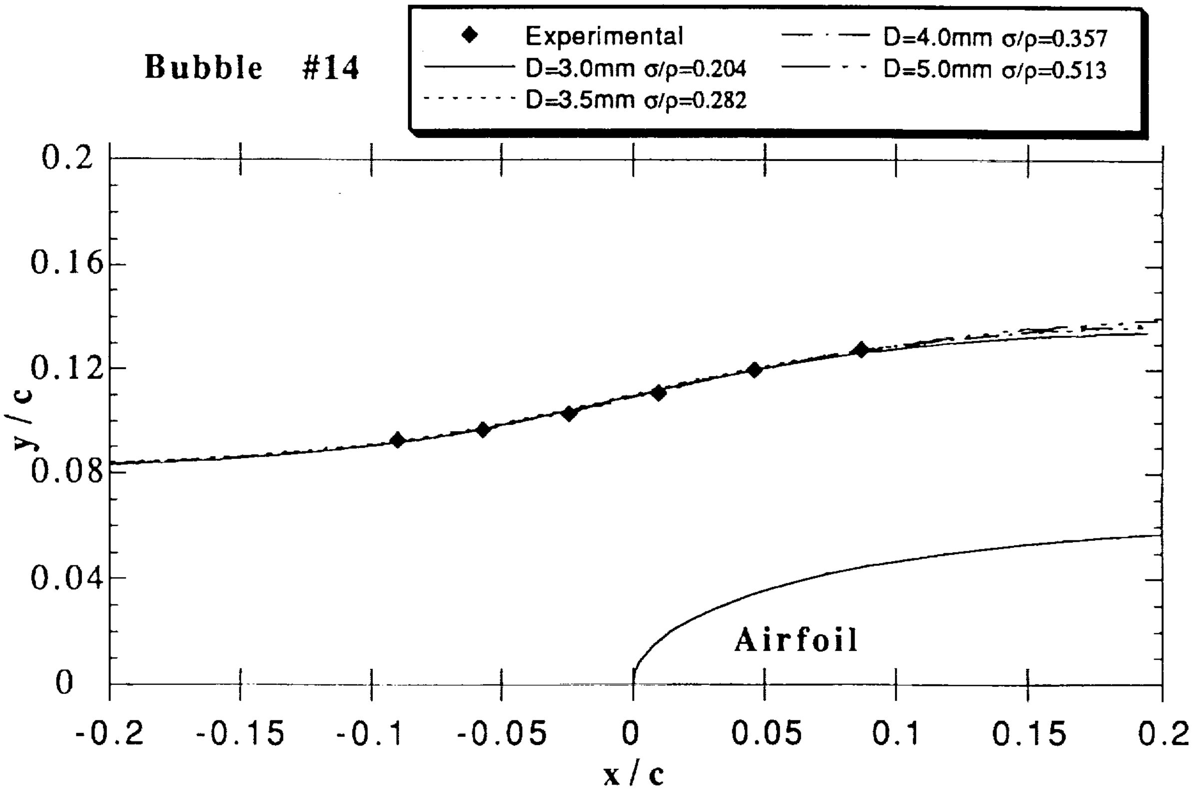
Bubble #14
◆ Experimental
D=3.0mm σ/ρ=0.204
D=3.5mm σ/ρ=0.282
D=4.0mm σ/ρ=0.357
D=5.0mm σ/ρ=0.513
y / c
0.2
0.16
0.12
0.08
0.04
0
-0.2
-0.15
-0.1
-0.05
0
0.05
0.1
0.15
0.2
x / c
Airfoil

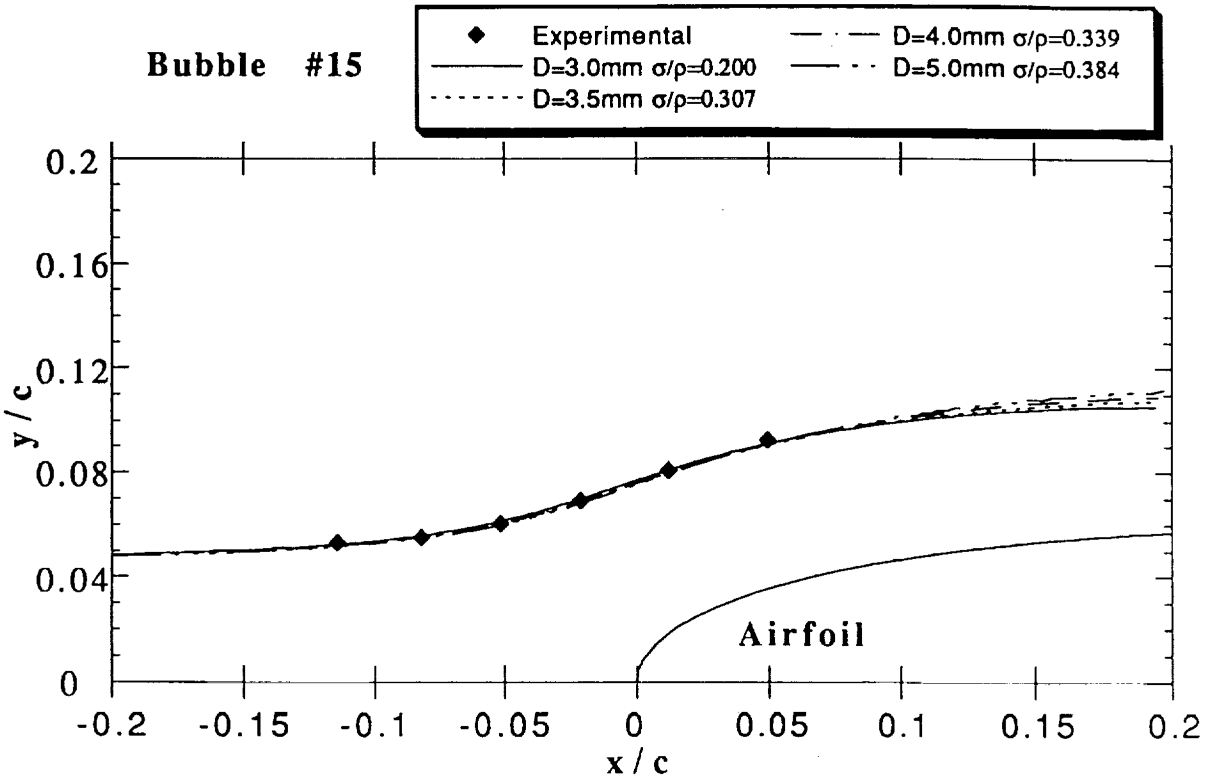
Bubble #15
Experimental
D=3.0mm σ/ρ=0.200
D=3.5mm σ/ρ=0.307
D=4.0mm σ/ρ=0.339
D=5.0mm σ/ρ=0.384
0.2
0.16
0.12
0.08
0.04
0
y / c
Airfoil
-0.2
-0.15
-0.1
-0.05
0
0.05
0.1
0.15
0.2
x / c

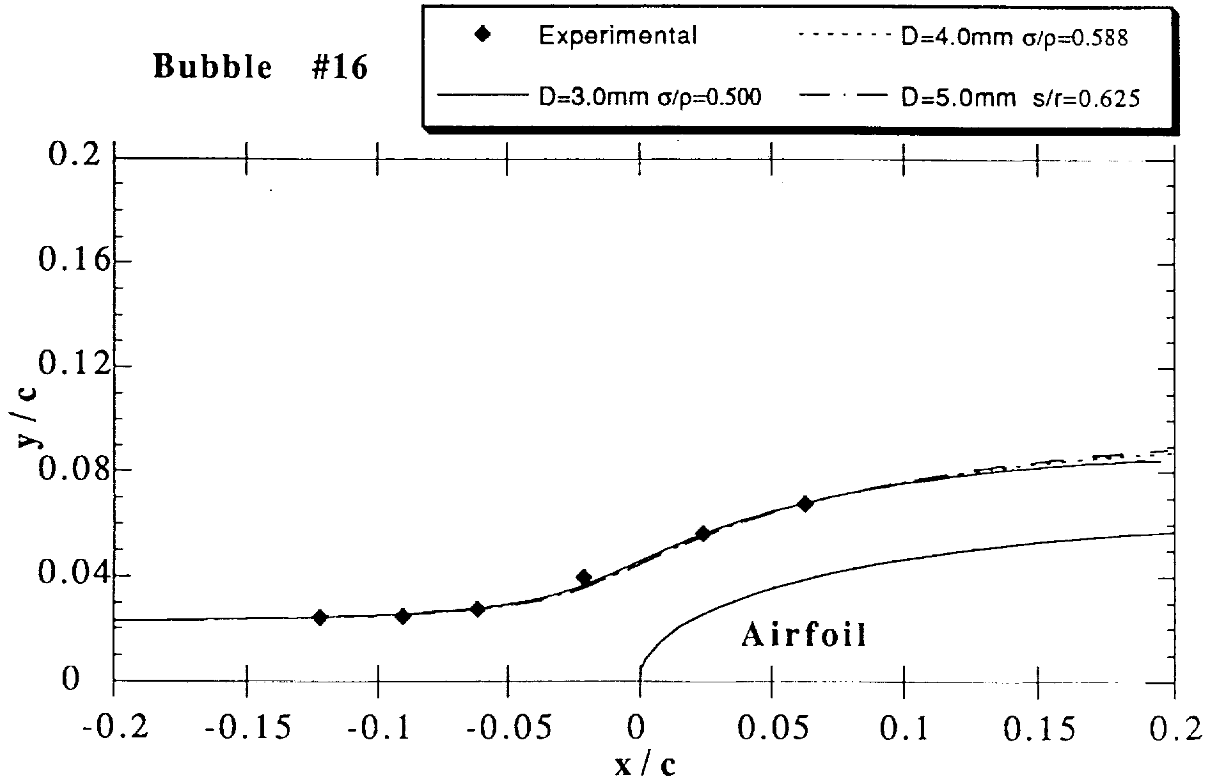
Bubble #16
Experimental
D=3.0mm σ/ρ=0.500
D=4.0mm σ/ρ=0.588
D=5.0mm s/r=0.625
0.2
0.16
0.12
0.08
0.04
0
y / c
Airfoil
-0.2
-0.15
-0.1
-0.05
0
0.05
0.1
0.15
0.2
x / c

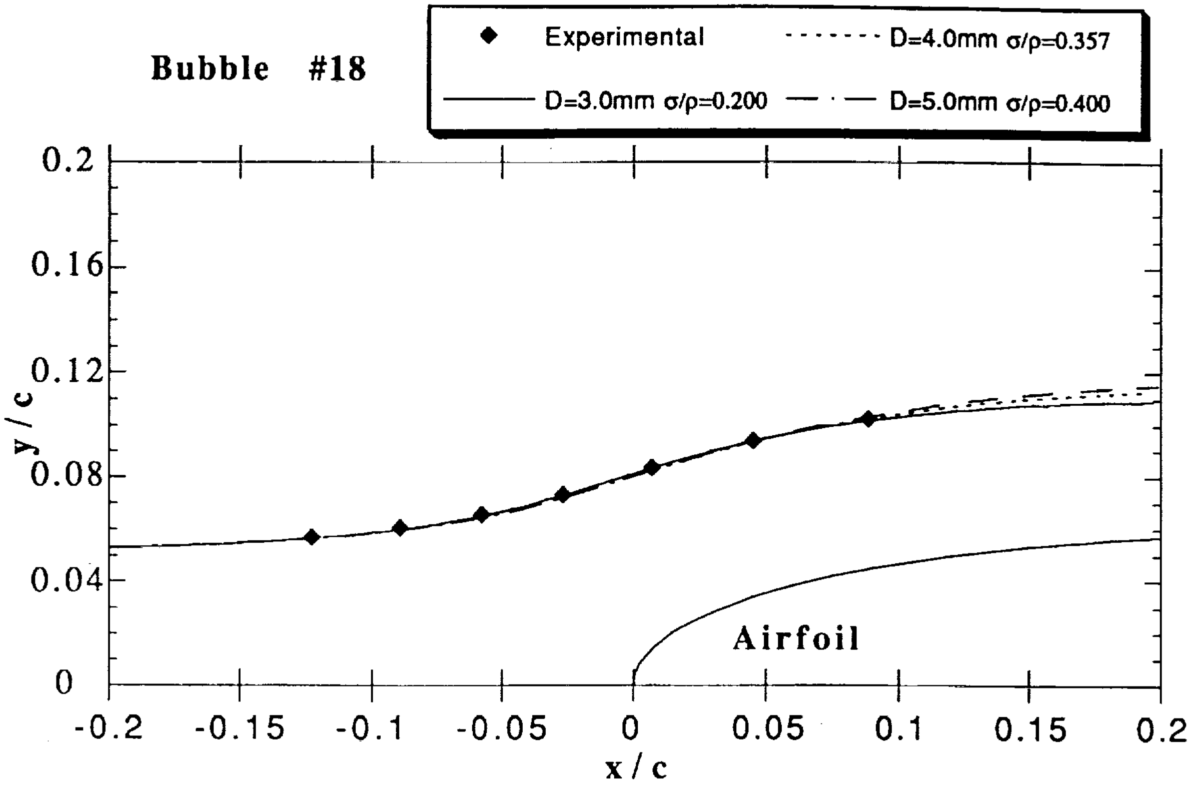
Bubble #18
Experimental
D=4.0mm σ/ρ=0.357
D=3.0mm σ/ρ=0.200
D=5.0mm σ/ρ=0.400
y / c
0.2
0.16
0.12
0.08
0.04
0
-0.2
-0.15
-0.1
-0.05
0
0.05
0.1
0.15
0.2
x / c
Airfoil

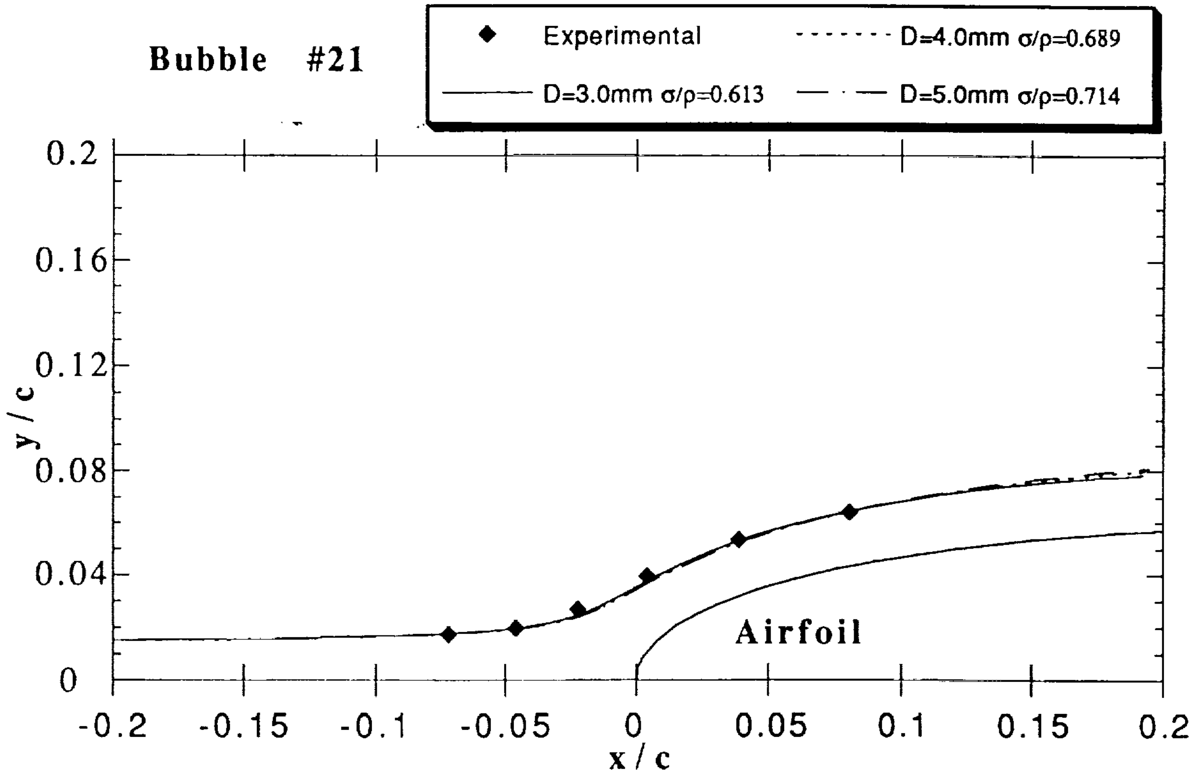
Bubble #21
Experimental
D=4.0mm σ/ρ=0.689
D=3.0mm σ/ρ=0.613
D=5.0mm σ/ρ=0.714
y / c
0.2
0.16
0.12
0.08
0.04
0
-0.2
-0.15
-0.1
-0.05
0
0.05
0.1
0.15
0.2
x / c
Airfoil

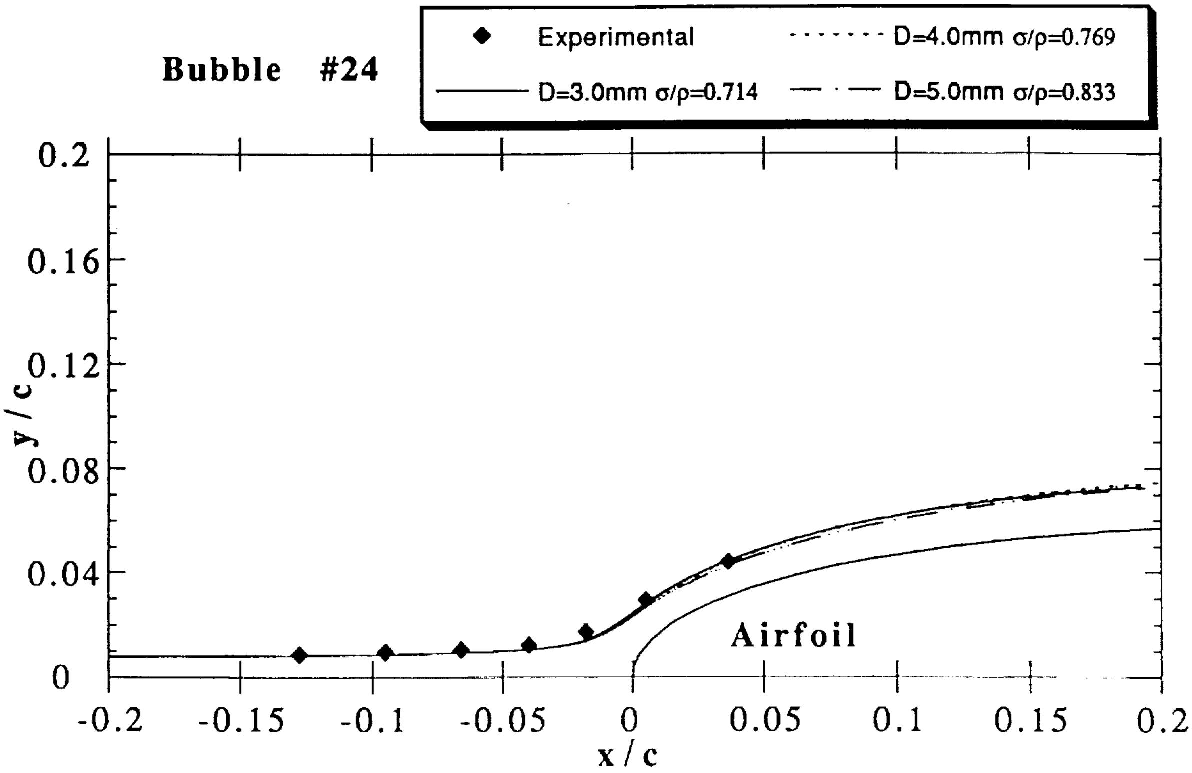
Bubble #24
◆ Experimental
D=3.0mm σ/ρ=0.714
D=4.0mm σ/ρ=0.769
D=5.0mm σ/ρ=0.833
0.2
0.16
0.12
0.08
0.04
0
y / c
-0.2
-0.15
-0.1
-0.05
0
0.05
0.1
0.15
0.2
x / c
Airfoil

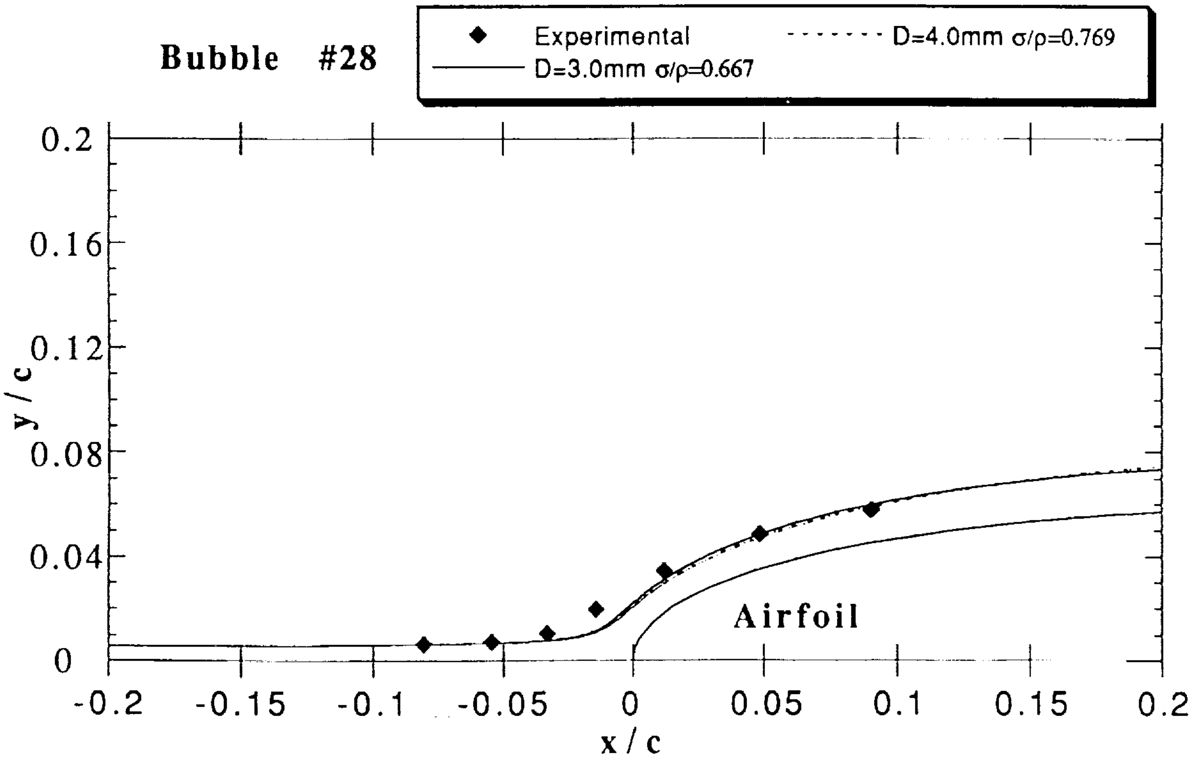
Bubble #28
◆ Experimental
D=3.0mm σ/ρ=0.667
D=4.0mm σ/ρ=0.769
0.2
0.16
0.12
0.08
0.04
0
y / c
-0.2
-0.15
-0.1
-0.05
0
0.05
0.1
0.15
0.2
x / c
Airfoil

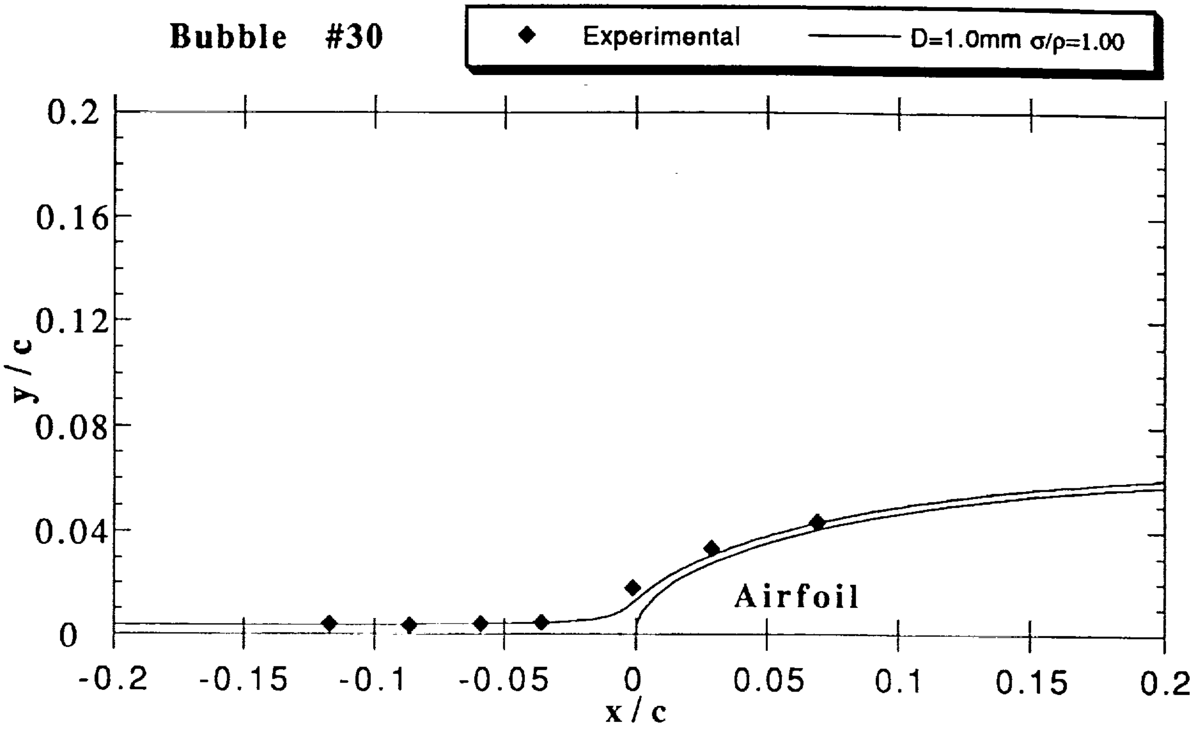
Bubble #30

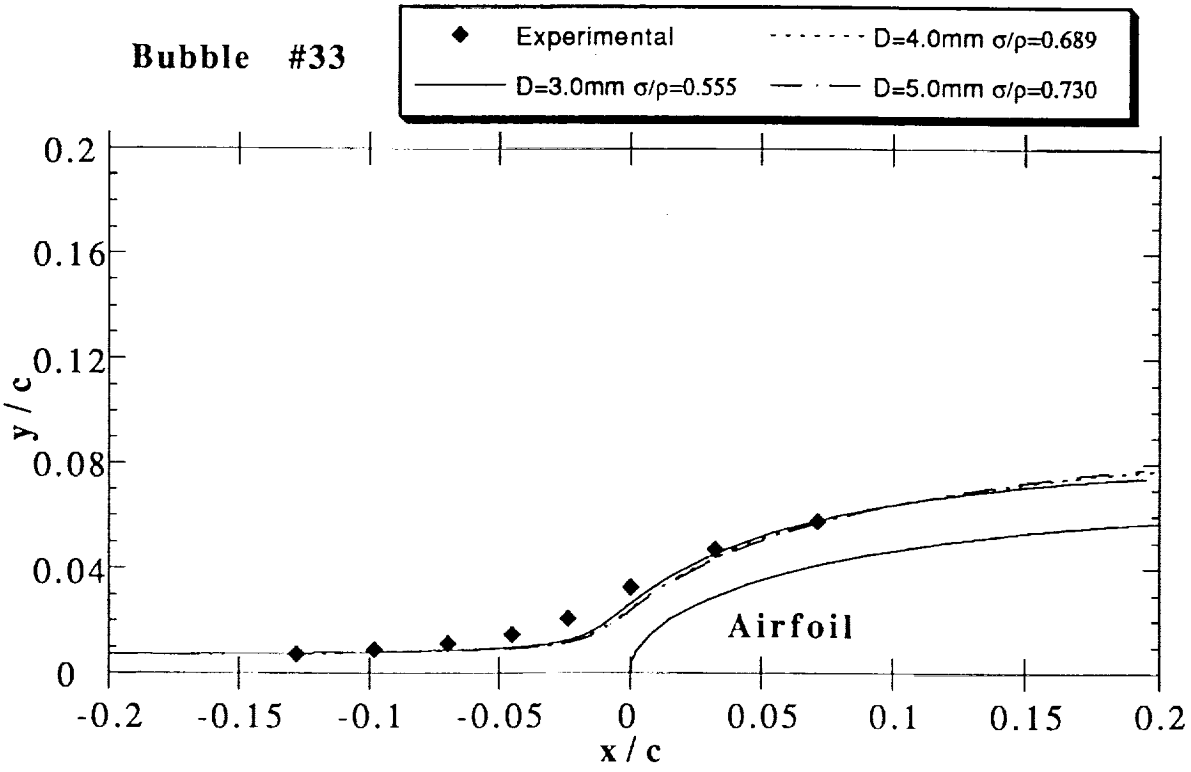
Bubble #33

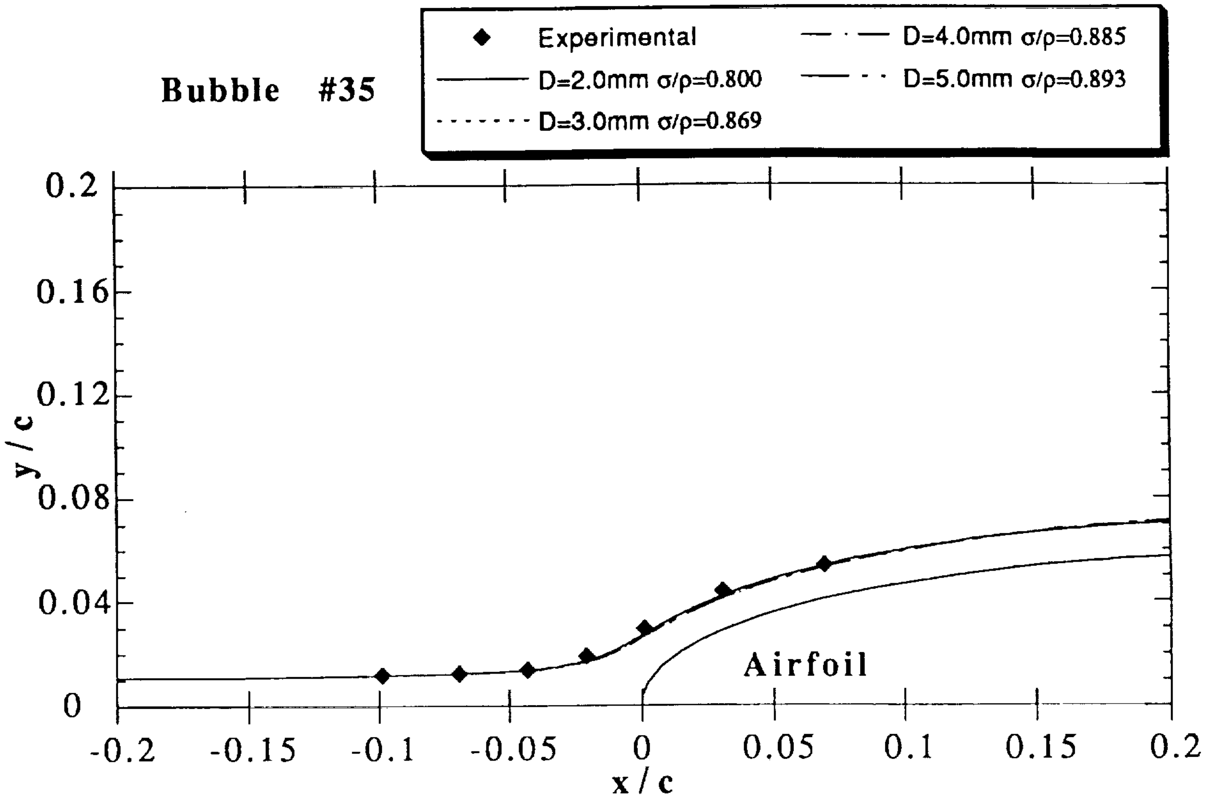Bubble #35
◆ Experimental
D=2.0mm σ/ρ=0.800
D=3.0mm σ/ρ=0.869
D=4.0mm σ/ρ=0.885
D=5.0mm σ/ρ=0.893
Airfoil
y / c
x / c
0.2
0.16
0.12
0.08
0.04
0
-0.2
-0.15
-0.1
-0.05
0
0.05
0.1
0.15
0.2

APPENDIX C

Analysis of The Vortex Filter:

The vortex filter operates by creating a vortex in a cylindrical tube with caps at both ends and a small hole in the center of one of the caps. Bubbles are injected tangentially at the wall into the filter. Only bubbles which are neutrally buoyant are reported to negotiate the vortex and spiral up and out the hole[3]. The general trends of the filter can be observed with a simple potential vortex. For this analysis, the equation of motion for a bubble will be reduced to equation (1C) for simplicity:

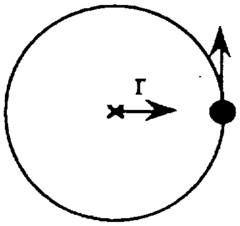

$$m_p \frac{dv_p}{dt} = \text{Force} = \frac{\pi D^3}{6} \nabla p$$

$$\frac{\pi D^3}{6} \sigma \frac{dv_p}{dt} = \frac{\pi D^3}{6} \nabla p$$

$$\frac{dv_p}{dt} = \frac{1}{\sigma} \nabla p \tag{1C}$$

We know that for a potential vortex $v = \Gamma/(2\pi r)$, and it can easily be shown that through the use of Bernoulli's equation the pressure gradient across the bubble can be written as:

$$\nabla p = \frac{1}{r}\frac{\partial p}{\partial r}\hat{\theta} + \frac{\partial p}{\partial r}\hat{r} = \frac{\partial p}{\partial r}\hat{r}$$

$$p = p_o - \frac{1}{2}\rho v^2 = p_o - \frac{1}{2}\rho\left(\frac{\Gamma}{2\pi r}\right)^2$$

$$\nabla p = \rho\left(\frac{\Gamma}{2\pi}\right)^2 \frac{1}{r^3} \tag{2C}$$

Letting $\tilde{\Gamma}=\Gamma/(2\pi)$ for convenience, the equation of motion of the bubble can be written as:

$$\frac{dv_p}{dt} = \frac{1}{\sigma/\rho}\left(\frac{\tilde{\Gamma}^2}{r^3}\right) \tag{3C}$$

For a mass of air moving around a potential vortex, the inertial force due to its centripetal acceleration balances the pressure force needed to maintain a perfectly circular path. The centripetal acceleration of the air produced by the vortex is equal to:

$$a_c = \frac{v^2}{r} = \frac{\left(\frac{\Gamma}{2\pi r}\right)^2}{r} = \frac{\tilde{\Gamma}^2}{r^3} \tag{4C}$$

Then rewriting eq.(1C) in terms of (2C) and a_c:

$$\frac{dv_p}{dt} = \frac{1}{\sigma/\rho}\, a_c \tag{6C}$$

Therefore, from the relationship of (6C):

$\frac{\sigma}{\rho} = 1$ (neutral) : $\frac{dv_p}{dt} = a_c \Rightarrow$ particle moves in a circle

$\frac{\sigma}{\rho} < 1$ (buoyant) : $\frac{dv_p}{dt} > a_c \Rightarrow$ particle moves towards center

$\frac{\sigma}{\rho} > 1$ (heavy) : $\frac{dv_p}{dt} < a_c \Rightarrow$ particle moves out towards wall

Bubbles with density ratios greater than one will move towards the wall of the filter and those with density ratios less than one will drawn to the center of the vortex. Therefore, since the actual apparatus expels the bubbles through a hole in the top center of the filter, those bubbles drawn to the center will be forced out of the filter. As a result, the filter screens out "heavy" bubbles and allows bubbles with density ratios of one or less, i.e. buoyant or neutrally buoyant bubbles to pass. The fact that no experimental bubbles with density ratios greater than one were recorded, adds strength to this argument.

REPORT DOCUMENTATION PAGE

Form Approved
OMB No. 0704-0188

1. AGENCY USE ONLY *(Leave blank)*

2. REPORT DATE
March 1993

3. REPORT TYPE AND DATES COVERED
Final Contractor Report

4. TITLE AND SUBTITLE
A Study of the Accuracy of Neutrally Buoyant Bubbles Used as Flow Tracers in Air

5. FUNDING NUMBERS
WU-505-68-10
NAG3-1134

6. AUTHOR(S)
Michael F. Kerho

7. PERFORMING ORGANIZATION NAME(S) AND ADDRESS(ES)
University of Illinois at Urbana-Champaign
Urbana, Illinois 61801

8. PERFORMING ORGANIZATION REPORT NUMBER
E-7630

9. SPONSORING/MONITORING AGENCY NAMES(S) AND ADDRESS(ES)
National Aeronautics and Space Administration
Lewis Research Center
Cleveland, Ohio 44135-3191

10. SPONSORING/MONITORING AGENCY REPORT NUMBER
NASA CR-191088

11. SUPPLEMENTARY NOTES
Project Manager, Mark G. Potapczuk, Propulsion Systems Division, (216) 433-3919.

12a. DISTRIBUTION/AVAILABILITY STATEMENT
Unclassified - Unlimited
Subject Category 02

12b. DISTRIBUTION CODE

13. ABSTRACT ***(Maximum 200 words)***

Research has been performed to determine the accuracy of neutrally buoyant and near neutrally buoyant bubbles used as flow tracers in air. Theoretical, computational, and experimental results are presented to evaluate the dynamics of bubble trajectories and factors affecting their ability to trace flow-field streamlines. The equation of motion for a single bubble was obtained and evaluated using a computational scheme to determine the factors which affect a bubble's trajectory. A two-dimensional experiment was also conducted to experimentally determine bubble trajectories in the stagnation region of a NACA 0012 airfoil at 0° angle of attack using a commercially available helium bubble generation system. Physical properties of the experimental bubble trajectories were estimated using the compational scheme. These properties included the density ratio and diameter of the individual bubbles. The helium bubble system was then used to visualize and document the flow field about a 30° swept semispan wing with simulated glaze ice. Results were compared to Navier-Stokes calculations and surface oil flow visualization. The theoretical and computational analysis have shown that neutrally buoyant bubbles will trace even the most complex flow patterns. Experimental analysis revealed that the use of bubbles to trace flow patterns should be limited to qualitative measurements unless care is taken to ensure neutral buoyancy. This is due to the difficulty in the production of neutrally buoyant bubbles.

14. SUBJECT TERMS
Aerodynamics; Flow visualization; Aircraft icing

15. NUMBER OF PAGES
84

16. PRICE CODE
A05

17. SECURITY CLASSIFICATION OF REPORT	18. SECURITY CLASSIFICATION OF THIS PAGE	19. SECURITY CLASSIFICATION OF ABSTRACT	20. LIMITATION OF ABSTRACT
Unclassified	Unclassified	Unclassified	

NSN 7540-01-280-5500

Standard Form 298 (Rev. 2-89)
Prescribed by ANSI Std Z39-18
298-102